

# Arecibo imaging of compact high-velocity clouds

W. B. Burton<sup>1</sup>, R. Braun<sup>2</sup>, and J.N. Chengalur<sup>3</sup>

<sup>1</sup> Sterrewacht Leiden, P.O. Box 9513, 2300 RA Leiden, The Netherlands

<sup>2</sup> Netherlands Foundation for Research in Astronomy, P.O. Box 2, 7990 AA Dwingeloo, The Netherlands

<sup>3</sup> National Centre for Radio Astrophysics, Post Bag 3, Ganeshkind PO, Pune, Maharashtra 411 007, India

Received mmdyy/ Accepted mmdyy

**Abstract.** Ten isolated compact high-velocity clouds (CHVCs) of the type cataloged by Braun & Burton (1999) have been imaged with the Arecibo telescope and were found to have a nested core/halo morphology. We argue that a combination of high-resolution filled-aperture and synthesis data is crucial to determining the intrinsic properties of the CHVCs. We identify the halos as Warm Neutral Medium surrounding one or more cores in the Cool Neutral Medium phase. These halos are clearly detected and resolved by the Arecibo filled-aperture imaging, which reaches a limiting sensitivity ( $1\sigma$ ) of  $N_{\text{HI}} \sim 2 \times 10^{17} \text{ cm}^{-2}$  over the typical  $70 \text{ km s}^{-1}$  linewidth at zero intensity. The FWHM linewidth of the halo gas is found to be  $25 \text{ km s}^{-1}$ , consistent with a WNM thermal broadening within  $10^4 \text{ K}$  gas. Substantial asymmetries are found at high  $N_{\text{HI}}$  ( $> 10^{18.5} \text{ cm}^{-2}$ ) levels in 60% of our sample. A high degree of reflection-symmetry is found at low  $N_{\text{HI}}$  ( $< 10^{18.5} \text{ cm}^{-2}$ ) in all sources studied at these levels. The column-density profiles of the envelopes are described well by the sky-plane projection of a spherical exponential in atomic volume density, which allows estimating the characteristic central halo column density,  $N_{\text{HI}}(0) = 4.1 \pm 3.2 \times 10^{19} \text{ cm}^{-2}$ , and characteristic exponential scale-length,  $h_B = 420 \pm 90 \text{ arcsec}$ . For plausible values of the thermal pressure at the CNM/WNM interface, these edge profiles allow distance estimates to be made for the individual CHVCs studied here which range between 150 and 850 kpc. An alternate method of distance estimation utilizing the mean exponential scale-length found in nearby low mass dwarf galaxies,  $h_B = 10.6 \pm 4.0 \text{ kpc}$ , yields distances in the range 320 to 730 kpc. A consequence of having exponential edge profiles is that the apparent size and total flux density of these CHVCs will be strongly dependent on the resolution as well as on the sensitivity of the data used; even a relatively deep observation with a limiting sensitivity of  $\sim 10^{19} \text{ cm}^{-2}$  over  $70 \text{ km s}^{-1}$  will detect only the central 30% of the source area and less than 50% of the total flux density. The exponential profiles also suggest that the outer envelopes of the CHVCs are not tidally truncated. Several CHVC cores exhibit a kinematic gradient, consistent with rotation. The halos appear kinematically decoupled from the cores, in the sense that the halos do not display the velocity gradients shown by the dense cores; the gradients are therefore not likely to be due to an external cause such as tidal shear. The much higher degree of symmetry observed in the halos relative to the cores also argues against an external cause of asymmetries in the cores.

**Key words.** ISM: atoms – ISM: clouds – Galaxy: evolution – Galaxy: formation – Galaxies: dwarf – Galaxies: Local Group

## 1. Introduction

There are two principal categories of the anomalous HI high-velocity cloud phenomenon. The first category, which contributes most of the emission flux, consists of low-contrast maxima of extended diffuse complexes with angular sizes up to tens of degrees. These complexes contribute a large fraction of the total HVC flux density observed; examples include the Magellanic Stream of debris from the Galaxy/LMC interaction (e.g. Putman & Gibson 1999) as well as some half-dozen extended HVC complexes (including complexes A, C, H, M, and oth-

ers). Although firm constraints on distances have been achieved only for a few of the complexes, the available distance determinations show these to lie rather nearby, at about 10 kpc (e.g. van Woerden et al. 1999). If, as seems plausible, the other large complexes also lie at distances ranging from several to some 50 kpc, they will have been substantially affected by the radiation and gravitational fields of the Milky Way. The second category of anomalous HI high-velocity clouds are the compact high velocity clouds (CHVCs, Braun & Burton 1999, hereafter BB99). CHVCs are intrinsically compact, isolated objects with angular sizes of about 1 degree. The spatial and kinematic distributions of the CHVCs were found to be consistent

with a dynamically cold ensemble spread throughout the Local Group, but with a net negative velocity with respect to the mean of the Local Group galaxies. This net negative velocity would imply an infall towards the Local Group barycenter at some  $100 \text{ km s}^{-1}$ .

The possibility that some of the high-velocity clouds might be essentially extragalactic has been considered in various contexts by, among others, Oort (1966, 1970, 1981), Verschuur (1975), Eichler (1976), Einasto et al. (1976), Giovanelli (1981), Bajaja et al. (1987), Wakker & van Woerden (1997), BB99, and Blitz et al. (1999). Blitz et al. revived the suggestion that high-velocity clouds are the primordial building blocks fueling galactic growth and evolution.

It is plausible to hypothesize that the high-velocity clouds may be viewed in terms of the hierarchical structure formation paradigm: the large HVC complexes would be nearby objects currently undergoing accretion onto the Galaxy, or representing tidal debris from a close encounter, while the compact, isolated CHVCs would be their distant counterparts, scattered throughout the Local Group environment. The accumulating support for such an hypothesis includes the evidence found by Helmi et al. (1999) in the Milky Way halo for a recently accreted dwarf galaxy, and the presence of the tidally disrupted Sagittarius dwarf galaxy (Ibata et al. 1994), which suggests stellar analogies to the extended HVC complexes; the theoretical simulations requiring numerous “mini-halo” systems (Klypin et al. 1999, Moore et al. 1999); as well as the relatively direct evidence regarding the distribution of some of the anomalous-velocity gas (Blitz et al. 1999, BB99). The CHVCs, which have a spatial and kinematic deployment similar to that of the Local Group dwarf galaxies, would represent inflowing material at substantial distances. Indications of internal star formation have not yet been found in CHVCs; if the objects are scattered throughout the Local Group, they have probably not yet been exposed to the Galactic radiation field or to strong external gravitational torques, and consequently the material would be in a less evolved form.

## 2. Motivation for filled-aperture observations

BB99 identified and confirmed a sample of 65 CHVCs. These objects evidently represent a more homogenous population than would a sample which included any of the major HVC complexes. The BB99 CHVC catalog was based on survey data made with telescopes of modest resolution. The primary source was the Leiden/Dwingeloo Survey (LDS) of Hartmann & Burton (1997), characterized by the angular resolution of  $36'$  provided by the Dwingeloo 25-meter telescope; at this resolution the CHVCs are largely unresolved.

Of the sample of 65 CHVCs cataloged, eight have been subject to high-resolution synthesis imaging. Wakker & Schwarz (1991) had used the Westerbork Synthesis Radio Telescope (WSRT) to show that both CHVC 114–06–466 and CHVC 114–10–430 exhibit a core/halo structure.

Subsequently Braun & Burton (2000, hereafter BB00) imaged six additional CHVC fields using the WSRT and showed that these objects also have a characteristic morphology whereby one or more quiescent, low-dispersion (linewidths in the range 2 to  $10 \text{ km s}^{-1}$  FWHM) compact cores (angular diameters typically 1 to 20 arcmin) are distributed over a region of some tens of arcmin extent, and are embedded in a diffuse, warmer halo of about one degree angular extent. We note that Cram & Giovanelli (1976) had earlier interpreted data, taken towards parts of an extended high-velocity cloud using the NRAO 300-foot and 140-foot telescopes, in terms of cold cores enveloped in warmer gas. However, that interpretation was based on the decomposition of complex line profiles into multiple Gaussian components, rather than direct observation of the individual components.

The high angular resolution of the WSRT data constitutes an important advantage in directly detecting the compact cores, but a particular disadvantage is inherent in synthesis data in detecting the diffuse halos. BB00 showed that the compact cores revealed so clearly in the WSRT data accounted for as little as 1% to only as much as 55% of the H I line flux detected in the single-dish LDS observations. The cores typically cover only some 15% of the source area. The high resolution of the synthesis data also allowed unambiguous identification of the core material with the cool condensed phase of the H I — the CNM — with kinetic temperatures near 100 K. However the diffuse structures extending over more than about 10 arcmin are not adequately imaged by the interferometer because of the missing short-spacing information.

BB00 attempted to account for this missing short-spacing information using the LDS material, but the sparseness of the total-power data supported only a crude correction. However, the data available for the CHVCs do suggest a characteristic two-phase structure, with the cores of CNM shielded by a halo of warm diffuse H I — the WNM — with temperatures near  $10^4 \text{ K}$  (corresponding to a thermal linewidth of about  $24 \text{ km s}^{-1}$  FWHM). Since the diffuse halos could not be detected convincingly and directly by the synthesis imaging, this nested geometry remained conjecture for the targeted objects. Direct detection of the diffuse halos was the principal motivation for undertaking the Arecibo observations reported here: these observations now provide the first resolved detection of the diffuse halos of the CHVCs, and confirm that the halos are the WNM gaseous phase providing a shielding column density for the CNM of the compact cores.

The Arecibo telescope is well-suited to provide sensitivity to the total column density at relatively high angular resolution. This issue is particularly important for CHVC targets, because they are of a size comparable to the primary beam of most synthesis instruments. The Arecibo data thus complement the interferometric data in a crucial manner.

**Table 1.** Compact, isolated high-velocity clouds observed at Arecibo. Column 1 gives the object designation; columns 2 and 3 give the celestial coordinates (J2000); column 4 gives the RMS sensitivity measured over  $10 \text{ km s}^{-1}$  on the wings of the constant-declination cross-cut; column 5 gives the velocity range over which the total  $N_{\text{HI}}$  was determined in this cross-cut; and column 6 gives the  $N_{\text{HI}}$  sensitivity, corresponding to the indicated RMS brightness and the velocity integration range.

Name	RA(2000)	Dec(2000)	RMS ( $10 \text{ km s}^{-1}$ )	$\Delta v$ ( $N_{\text{HI}}$ cut)	$N_{\text{HI}}$ RMS
CHVC $lll \pm bb \pm vvv$	(h m)	( $^{\circ} \prime \prime$ )	(mK)	( $\text{km s}^{-1}$ )	( $10^{17} \text{ cm}^{-2}$ )
CHVC 092-39-367	23 14.0	17 24 00	6.5	86	3.4
CHVC 100-49-383	23 50.5	11 19 00	4.6	63	2.1
CHVC 148-32-144	02 26.5	26 22 30	11.0	63	5.0
CHVC 158-39-285	02 41.5	16 17 30	3.8	86	2.0
CHVC 186-31-206	04 14.0	06 36 19	14.0	58	6.1
CHVC 186+19-114	07 17.5	31 52 00	5.9	75	2.9
CHVC 198-12-103	05 42.0	07 54 00	3.9	75	1.9
CHVC 202+30+057	08 27.0	21 46 00	7.0	65	3.2
CHVC 204+30+075	08 27.0	20 01 30	5.4	72	2.6
CHVC 230+61+165	10 55.0	15 28 30	5.8	80	3.0

### 3. Sample selection

Ten examples of the compact, isolated high-velocity clouds of the type cataloged by BB99 were selected for the Arecibo observations. The targets are listed by their CHVC designation in Table 1. Nine of the sources had been identified in the BB99 compilation. The tenth source, CHVC 186-31-206, is evident in the LDS but it had not been included in the BB99 list because it appears in the same general area of the sky as the Anticenter Stream complex and therefore had been excluded by the isolation criterion of BB99. The new, higher-quality Arecibo data suggest that this source is sufficiently compact and isolated in velocity to be placed in the CHVC category. Three of the ten objects selected also occur in the Wakker & van Woerden (1991) catalog, namely CHVC 158-39-285 (WvW486), CHVC 186+19-114 (WvW 215), and CHVC 198-12-103 (WvW 343), the others having evidently passed undetected through the relatively coarse gridding lattice of the data on which the Wakker & van Woerden catalog was based. The targets selected span both negative and positive radial velocities, and occur in both the northern and southern Galactic hemispheres. Consistent with the operational definition of the CHVC class of objects, the sources observed at Arecibo were only marginally resolved in the 36-arcmin beam of the Dwingeloo telescope.

## 4. Observations

### 4.1. Instrumental parameters

The observations were carried out during seven days in November, 1999, using the Gregorian feed together with the narrow L-band (LBN) receiver.

The spherical primary of the Arecibo telescope is 305 meters in diameter; the Gregorian optics comprises two subreflectors, illuminating the primary over an area of about  $210 \times 240$  meters in extent. The FWHM beamwidth

measured with the wide L-band (LBW) feed at 1420 MHz is  $3.1 \times 3.7$  arcmin in the azimuth and zenith-angle directions, respectively (Heiles 1999). Measurements for the LBN feed (Howell 2000) yield values consistent with that of the LBW feed. Different sections of the spherical reflector are illuminated, however, depending on the source position. In order to minimize beam distortions and gain variations caused when the illuminated pattern spills over the edges of the primary surface, we constrained most of the observations to moderate zenith angles, less than  $17^{\circ}$ . The pointing accuracy of the telescope system is about  $5''$ , and thus of no concern for the extended sources observed in our program. The observations were carried out during the period extending from local sunset until about two hours after sunrise, shown by experience to provide the most stable baselines.

The spectrometer was a 9-bit 2048 channel autocorrelator observing two polarizations with two simultaneous bandpass settings, namely 6.25 MHz and 1.56 MHz, yielding  $\Delta v = 1.3$  and  $0.32 \text{ km s}^{-1}$ , respectively. The bands were centered on the  $v_{\text{LSR}}$  of the CHVC targets as determined by BB99 for 9 of the 10 targets, and from observations from the LDS for CHVC 186-31-206.

### 4.2. Observing and calibration strategy

Each of the CHVC targets was first mapped on a grid of  $1^{\circ} \times 1^{\circ}$  size on a fully-sampled 90 arcsec lattice, but using short integrations, in order to determine the locations of the peak flux concentrations and derive a nominal gain calibration for the field based on the background continuum sources. Each Nyquist-sampled  $1^{\circ} \times 1^{\circ}$  map involved 73 minutes of effective integration time. The average of the first and last 90-arcsec of RA of each data-scan were used to calibrate the passband shape of each spectrum in that scan. In the event that source emission extends to the edges of the sampled region in RA, this will lead to a weighting down of such features. This pos-

sibility must be borne in mind in the subsequent analysis. An estimate of the continuum emission was then constructed by averaging in frequency over the line-free data. Spatial Gaussian fits were made to compact and unconfused continuum sources which were present by chance in the observed fields. Comparison with the same sources detected in the NVSS (Condon et al. 1998) allowed determination of a nominal absolute gain calibration factor for each field. Typically, several suitable sources with flux densities in the range of 100–200 mJy were present. The derived noise-equivalent flux density (NEFD, or  $T_{\text{Sys}}/\text{Gain}$ ) averaged over all observed fields was  $3.30 \pm 0.26$  Jy. While a small systematic variation (of about 5%) in NEFD is expected with zenith angle, we chose to adopt the NEFD derived from each fully-sampled image to calibrate all of the subsequent drift-scan data acquired for that field. The relationship between flux density and brightness temperature follows from the beam area at 1420 MHz,  $S(\text{Jy}/\text{Beam}) = 0.0634 T_{\text{B}}(\text{K})$ .

These shallow images then served as finding charts on which to identify the principal flux concentrations. Longer-integration spectra were then accumulated in a single cross-cut made at constant declination by repeating drift scans of  $2^\circ$  length centered on this peak. As many as 75 constant-declination driftscans were accumulated for some of the objects, providing integration times of as much as 15 minutes per beam. As with the mapping data, the first and last 90 arcsec of each scan in RA were averaged to perform the initial calibration of the passband shape. A spatial smoothing in the RA direction with a 180 arcsec Gaussian was employed to enhance the signal-to-noise figure with only a modest degradation of spatial resolution. Various smoothings were employed in the velocity direction to enhance detection of low-surface-brightness emission features. On the basis of the final averaged and smoothed data, the off-source ranges of RA and velocity were determined. The off-source range of RA was used to form an average spectrum for a final passband calibration. The off-source range of velocity was used to determine the average continuum level to subtract from each spectrum. No other baseline manipulation was employed.

The resulting RMS sensitivities over  $10 \text{ km s}^{-1}$ , as indicated in column 4 of Table 1, were as low as 4 mK; this limit corresponds to sensitivity to H I column density, after summing over the typical,  $70 \text{ km s}^{-1}$ , emission linewidth at zero intensity, of  $2 \times 10^{17} \text{ cm}^{-2}$ . The resulting H I material constitutes the most sensitive yet obtained for high-velocity clouds. This sensitivity is particularly important for determining the properties of the diffuse halos, largely inaccessible in synthesis data.

### 4.3. Observational displays

The observational material is displayed as follows.

The panel on the upper left in each of Figs. 1 through 10 shows contours of integrated intensity for the shallow  $1^\circ \times 1^\circ$  images made of each of the CHVC targets.

These moment-map panels show the integrated H I column depth at the contour levels, in units of  $10^{18} \text{ cm}^{-2}$ , indicated below each panel, with the range of integration given in the column 5 of Table 1. The contour plot on the upper right in each of Figs. 1–10 shows the intensity-weighted velocity field as determined from the data in the integrated-flux map. The contours give the intensity-weighted  $v_{\text{LSR}}$ , at the levels indicated below the panel.

The panels in the lower portion of the various Figs. 1 through 10 refer to the deep driftscan material accumulated over  $2^\circ$  at a central declination chosen for each CHVC. The panel on the lower left in each of the figures shows the resulting position, velocity map for each target at a velocity smoothing of  $10 \text{ km s}^{-1}$  FWHM. The constant declination along which the deep driftscan was made is indicated above each of these panels; the contours give the intensities in units of mK, at the levels indicated below each panel. The panels adjacent to the  $\alpha, v_{\text{LSR}}$  cuts show (from upper to lower, respectively) the  $v_{\text{LSR}}$  of the emission centroid measured along the cut, the velocity FWHM of the emission, and the logarithm of  $N_{\text{HI}}$  measured along the constant- $\delta$  cross-cut. These properties were determined from the region indicated by the vertical lines in the adjacent position, velocity diagram. This velocity range was chosen to encompass as much as possible of the detected H I emission from each object while excluding any confusing features.

Several of the position, velocity cross-cuts display a kinematic gradient, but it is important to remain aware that the longer-integration cross-cuts refer to a single slice, in a specific orientation, through a particular emission concentration, across a CHVC which may in fact comprise multiple cores. Until the data can be improved such that the entire object is imaged deeply, the shallow images shown in the upper panels of the relevant figure must be consulted to judge if this gradient is aligned with a possible elongation of the spatial map or with possible kinematic gradients seen in the larger context.

The plots in Figs. 11 and 12 show the variation of  $N_{\text{HI}}$  with radius measured from the position of peak column density in the single deeper-integration cross-cut made across each of the CHVC targets. The RMS sensitivities (measured over  $10 \text{ km s}^{-1}$ ) of these slices are indicated in column 4 of Table 1; the total velocity extents over which the column depths were determined are indicated in column 5 of the table. The plots of  $N_{\text{HI}}$  against radius were truncated at a level of 2 times the RMS value. The Eastern and Western halves of the CHVCs are plotted separately in the panels of Fig. 11 and 12, in order to allow assessment of the reflection-symmetry seen in the two halves of the cross-cut. Since the choice of origin is arbitrary, it is the profile slope at a given column density which should be compared rather than simply the degree of overlap with this particular choice of origin. The dotted curve overlaid on each of the panels is described below.

The plots in Figs. 13 and 14 show the  $T_{\text{B}}, v_{\text{LSR}}$  spectrum measured in the direction of the column density peak identified in the long-integration driftscans shown

in the panels on the lower left of Figs. 1–10. Overlaid on each spectrum (at  $1 \text{ km s}^{-1}$  velocity resolution) is the profile representing a Gaussian fit. A single Gaussian was fit to all of the profiles except for the one observed for CHVC 186+19–114, for which two Gaussians were judged inevitable. Note that the information for each CHVC represented in this figure refers only to a single line-of-sight toward one peak, namely the peak of the emission centroid chosen for the cross-cut.

## 5. Results for the selected CHVCs

We briefly summarize the structural and kinematic data obtained for each of the ten observed fields. We first comment on the appearance of each object in the shallow Nyquist-sampled  $1^\circ \times 1^\circ$  grids and in the deeper integrations along the two-degree cross-cut, as shown in the respective panels of Figs. 1–10, and then comment on the spatial and kinematic properties of one of the principal cores of each CHVC, as shown in the respective panels of Figs. 11 and 12 and Figs. 13 and 14. Some of the results are summarized in Table 2.

### 5.1. CHVC 092–39–367

CHVC 092–39–367 is one of the weaker objects in the BB99 catalog, but one at a relatively extreme negative radial velocity. With the  $3\text{'}/5$  angular resolution of the Arecibo telescope, the feature shows a complex core/halo morphology. The two-dimensional shallow-mapping image, shown in the upper left of Fig. 1, reveals an ensemble of some half dozen separate cores, largely embedded in extended emission. The velocity centroids of the individual cores range between  $v_{\text{LSR}} = -350$  and  $-370 \text{ km s}^{-1}$ . The  $1^\circ \times 1^\circ$  image in the upper-left panel shows no well-defined structural axis, and the intensity-weighted velocity field of this two-dimensional image, shown in the panel on the upper-right of Fig. 1, also shows no well-defined kinematic pattern.

The longer-integration driftscan cross-cut spanned two degrees of right ascension at  $\delta = 17^\circ 24'$ . This declination was chosen because it crosses the core with the highest column density; but it will be clear that a cross-cut at a different constant declination, i.e. crossing a different region of the CHVC, might reveal different details. The cross-cut, displayed as an  $\alpha, v_{\text{LSR}}$  map in the lower left of Fig. 1, shows two of the brighter cores evident in the moment-map image, as well as one of the fainter cores evident in the two-dimensional image, but also an additional minor core feature which is out of the field of view of the  $1^\circ \times 1^\circ$  image. With the higher sensitivity of the longer integration, all four of these cores are revealed to be embedded in a common envelope.

The three panels grouped on the lower right of Fig. 1 show the  $v_{\text{LSR}}$ , the velocity FWHM, and the logarithm of

$N_{\text{HI}}$ , as measured along the constant-declination cross-cut. The data show an overall kinematic gradient spanning about  $20 \text{ km s}^{-1}$  over the  $1.5$  degree extent of the entire source. Superposed on this global gradient are the much more abrupt gradients associated with the individual compact cores. These abrupt gradients reach magnitudes of  $10\text{--}15 \text{ km s}^{-1}$  on scales of only  $5\text{--}10$  arcmin.

The FWHM velocity width varies between about  $25 \text{ km s}^{-1}$ , in unconfused regions, and  $40 \text{ km s}^{-1}$ , in those regions where different components overlap along the line-of-sight. (We comment below on the interpretation of these FWHM values, which, of course, represent upper limits to the *in situ* kinematics.) The column depths of the two principal cores are about  $10^{19.3} \text{ cm}^{-2}$ ; the diffuse envelope in which the cores are embedded has been traced to  $N_{\text{HI}}$  levels of about  $10^{18.0} \text{ cm}^{-2}$ .

The panel on the upper left in Fig. 11 shows the variation of  $\log(N_{\text{HI}})$  with angular distance from the peak column density, separately for the Western and Eastern halves of the object. The column depths can be traced on both halves to levels somewhat less than  $10^{18} \text{ cm}^{-2}$ , at an angular distance of some  $45'$  from the emission centroid of the constant- $\delta$  slice. The panel on the upper left in Fig. 13 represents a  $T_{\text{B}}, v_{\text{LSR}}$  spectrum through the emission centroid. Overlaid on the spectrum is a Gaussian distribution corresponding to the  $v_{\text{LSR}}, T_{\text{max}}$ , and FWHM parameters listed in Table 2.

### 5.2. CHVC 100–49–383

CHVC 100–49–383, like the previous object also at an exceptionally extreme velocity, appears in the BB99 catalog as a particularly simple object. The confirming data sought by BB99 had involved additional data from the Dwingeloo 25-m telescope, Nyquist-sampled on a  $15'$  grid. The Arecibo  $1^\circ \times 1^\circ$  mapping image shown in the upper left of Fig. 2 shows considerably more detail at this higher resolution and greater sensitivity: the brightest core is offset to the North-East of the source centroid, while secondary cores are distributed over a wider region and are all embedded in a common envelope.

The deeper cross-cut shown in the lower left of Fig. 2 scans the  $2^\circ$  strip along the declination,  $11^\circ 19'$ , where the brightest core is most intense. There is only a modest velocity gradient along this cut, amounting to less than  $10 \text{ km s}^{-1}$ . However, within the bright core there are rapid velocity reversals on scales of  $5\text{--}10$  arcmin. The velocity FWHM varies between about  $25$  and  $35 \text{ km s}^{-1}$ . The core peaks at a column depth of  $10^{19.9} \text{ cm}^{-2}$ . The envelope could be followed on the lower- $\alpha$  side to  $N_{\text{HI}} \sim 10^{18.3} \text{ cm}^{-2}$ .

A noteworthy aspect of the morphology of this CHVC is that the off-center location of the brightest core component gives it the appearance of being more sharply bounded on one side than the other. The panel on the upper right of Fig. 11 shows the column density profiles to the East and West of the position of the bright core. While

**Table 2.** CHVC properties. Column 1 gives the object designation. Columns 2, 3, and 4 give the  $v_{\text{LSR}}$ , the peak temperature, and the velocity FWHM, respectively, determined from the Gaussian fits (plotted in Figs. 13 and 14) to the emission peaks of the deep constant-declination driftscans. Column 5 gives the logarithm of the H I column density in the direction of the emission peak, integrated over the velocity ranges limited by the vertical lines in the panels on the lower left of Figs. 1–10. Columns 6 and 7 give the total WNM atomic column density and exponential scale-length, respectively, derived as discussed in the text under the assumption of approximate spherical symmetry. Column 8 gives the distance calculated from eqn.4 and a nominal CNM/WNM transition pressure. Column 9 gives the distance calculated assuming a mean outer disk scale-length,  $h_B=10.6$  kpc, as found for nearby low mass dwarf galaxies.

Name	$v_{\text{LSR}}$ ( $\text{km s}^{-1}$ )	$T_{\text{max}}$ (K)	FWHM ( $\text{km s}^{-1}$ )	$\log(N_{\text{HI}})$ Gauss-fit	$\log(N_{\text{HI}}(0))$ halo-fit	$h_B$ (arcsec)	Dist. (eqn.4) (kpc)	Dist. ( $h_B=10.6$ kpc) (kpc)
CHVC 092–39–367	–358	0.5	25	19.4	19.4	300	280	730
CHVC 100–49–383	–395	1.5	26	19.9	19.4	350	—	—
CHVC 148–32–144	–156	1.3	13	19.6	19.3	250	—	—
CHVC 158–39–285	–285	0.5	23	19.4	19.4	550	150	400
CHVC 186–31–206	–206	1.3	22	19.7	19.6	500	270	440
CHVC 186+19–114	–118	5.9	12	20.1	20.0	400	840	550
	–115	3.4	3.5	19.4				
CHVC 198–12–103	–102	1.7	22	19.9	19.7	400	420	550
CHVC 202+30+057	+60	4.5	21	20.3	20.0	450	740	490
CHVC 204+30+075	+69	2.7	26	20.1	19.5	100	—	—
CHVC 230+61+165	+155	0.4	26	19.3	19.2	350	150	320

the Eastern profile shows a rapid decrease in  $N_{\text{HI}}$  to values below  $10^{18} \text{ cm}^{-2}$ , corresponding to the actual edge of the source, we detect emission in excess of  $10^{18} \text{ cm}^{-2}$  out to the limit of our coverage in the West. Only by extending the coverage significantly further to the West would it become clear whether the WNM halo in this source is itself symmetric or not. Similar off-center locations of bright cores are seen in several of the other CHVCs described here, and are discussed further below. The spectrum corresponding to the peak of the deep driftscan and plotted on the upper right of Fig. 13 indicates that the CNM core shows substantial kinematic symmetry.

### 5.3. CHVC 148–32–144

CHVC 148–32–144 appears in the BB99 catalog as a simple, but somewhat elongated object, at a modest deviation velocity. The Arecibo  $1^\circ \times 1^\circ$  shallow image shown in the upper left of Fig. 3 does not fully encompass the CHVC; two prominent cores are evident in the region mapped, each having — as shown in the intensity-weighted velocity field image of the upper right panel — its own characteristic velocity. The cores are enclosed in a common envelope. The constant declination for the deeper  $2^\circ$  cross-cut was chosen at  $\delta = 26^\circ 22'$ , near one of the peaks in the shallow image.

The deep constant-declination driftscan through the CHVC is shown in the lower left of Fig. 3. In this direction, two intensity peaks are seen, the principal one centered near  $\alpha = 2^{\text{h}}26^{\text{m}}40^{\text{s}}$  and  $v_{\text{LSR}} = -155 \text{ km s}^{-1}$ , and a secondary one near  $\alpha = 2^{\text{h}}23^{\text{m}}30^{\text{s}}$  and  $v_{\text{LSR}} = -140 \text{ km s}^{-1}$ . It is plausible that the rather large velocity FWHM of  $35 \text{ km s}^{-1}$  tabulated for this object by BB99 on the basis of

mapping with the Dwingeloo 25-m telescope refers to the accumulated kinematics contributed by several cores, each at a somewhat different centroid velocity. Thus the principal core measured in the Arecibo data has a FWHM of  $17 \text{ km s}^{-1}$ , whereas the secondary core has a FWHM of about  $25 \text{ km s}^{-1}$ .

The cross-cut slice through CHVC 148–32–144 shows that this object also is characterised by a spatial offset of the brighter core from the centroid of the underlying halo. Only on the Eastern side of the source does the coverage extend far enough to adequately sample the edge where it can be followed to column depths as low as some  $10^{17.7} \text{ cm}^{-2}$ , at  $\sim 6'$  from the bright core. The middle panel on the left of Fig. 13 shows a single-Gaussian fit to the spectral cut through the CHVC. The residuals from the single-Gaussian fit are substantially greater than the noise level, and are systematic in nature: evidently this CHVC has spatial structure which is essentially unresolved in angular extent at the limit of the Arecibo data.

### 5.4. CHVC 158–39–285

CHVC 158–39–285, at a substantial negative velocity, is one of the faintest in the catalog of BB99. The  $1^\circ \times 1^\circ$  two-dimensional Arecibo image shown in the upper left of Fig. 4 reveals a core of higher column density H I emission, surrounded by additional sub-structure. The velocity field shown in the upper right of Fig. 4 shows a systematic kinematic gradient oriented East-West along the long axis of the brightest portion of the object.

The more sensitive observations constituting the  $2^\circ \alpha, v_{\text{LSR}}$  cross-cut through the core were made at  $\delta = 16^\circ 17' 30''$ . The  $N_{\text{HI}}$  value reaches some  $10^{19.4} \text{ cm}^{-2}$  at

the peak of the core.  $N_{\text{HI}}$  in the diffuse envelope can be traced to about  $10^{17.6} \text{ cm}^{-2}$  on the Western side, where the centroid velocity is some  $20 \text{ km s}^{-1}$  different from the velocity characteristic of the peak of the core emission. The spatial coverage to the East is not sufficient to reach the edge of the envelope.

The position, velocity cross-cut reveals a clear kinematic gradient within the high column density core of this source, spanning a velocity difference of  $30 \text{ km s}^{-1}$ , and possibly suggesting rotation in a flattened disk. Because of its interesting kinematic structure and limited angular extent, this core is a good candidate for synthesis mapping.

The panel on the middle right of Fig. 11 shows the  $N_{\text{HI}}$  profiles to the East and West of the position of peak column density. The two edge profiles are remarkably symmetric over the measured range of column density. The panel on the middle right of Fig. 13 shows that a single Gaussian accounts for much of the emission.

### 5.5. CHVC 186–31–206

CHVC 186–31–206, not previously identified as a high-velocity cloud, shows an elongated structure in the two-dimensional shallow image on the upper left of Fig. 5, with one principal core and at least two secondary ones, enclosed in a common envelope. The velocity field shown on the upper right of the figure shows that the different core substructures of this CHVC occur at different characteristic velocities, spanning some  $12 \text{ km s}^{-1}$ . The velocity gradient oriented along the elongated axes of the feature might suggest rotation.

The declination for the longer-integration cross-cut was chosen to coincide with the peak of the CHVC flux, at  $6^{\circ}36'19''$ . The emission along this slice peaks at a velocity of  $-206 \text{ km s}^{-1}$ . The envelope can be followed to  $N_{\text{HI}}$  levels of somewhat less than  $10^{18} \text{ cm}^{-2}$ .

The panel shown on the lower left of Fig. 11 indicates that while the Eastern edge of this CHVC has been delineated to below  $N_{\text{HI}}=10^{18} \text{ cm}^{-2}$ , the coverage has not been sufficient to fully characterize the Western edge. The fit by a single Gaussian shown in the corresponding panel of Fig. 13 shows residuals of greater amplitude than expected from the noise figure of the data: this object might have structure which remains unresolved in angle by the Arecibo beam. (The results obtained for the few CHVCs which have been observed both at Arecibo and with the WSRT show that it is eminently plausible to expect such unresolved structure at the Arecibo resolution.)

### 5.6. CHVC 186+19–114

CHVC 186+19–114 is one of the brighter ( $T_{\text{max}} = 1.03 \text{ K}$  in the LDS) objects in the CHVC tabulation of BB99. The shallow Arecibo image shows an elongated structure, extending beyond the limits of the  $1^{\circ} \times 1^{\circ}$  map shown on the upper left of Fig. 6. The panel on the upper right of

this figure shows that the centroid velocity on the lower- $\delta$  side is some  $10 \text{ km s}^{-1}$  less extreme than on the higher- $\delta$  side.

The declination for the  $2^{\circ}$  longer-integration cross-cut was chosen to coincide with the peak column density, at  $31^{\circ}52'$ . The structure revealed by the observations along this slice is that of an elongated core. But the emission sampled in the constant- $\delta$  cut is probably not contributed by a single, simple core. The panel in the upper left of Fig. 12 shows the two opposing  $N_{\text{HI}}$  profiles which can be traced only down to about  $10^{18} \text{ cm}^{-2}$ . The corresponding panel in Fig. 14 shows that the kinematics measured through the core can not be fit by a single Gaussian, but requires (at least) two features to account for the shape of the spectrum. The emission on the wings of the spectrum remaining unaccounted for by a two-component fit suggests that the core/halo morphology which seems characteristic of CHVCs imaged at high resolution by the WSRT pertains here too, with the Arecibo resolution only marginally sufficient to resolve the core/halo structure.

### 5.7. CHVC 198–12–103

CHVC 198–12–103 appears in the BB99 catalog as a moderately bright ( $T_{\text{max}} = 0.48 \text{ K}$ ), broad feature with a rather simple form. This impression remains under more detailed scrutiny with the Arecibo telescope. The  $1^{\circ} \times 1^{\circ}$  imaging data shown on the upper left of Fig. 7 reveals a highly asymmetric core component with some internal sub-structure. The core is characterized by a much sharper gradient to the East than to the West. The intensity-weighted velocity centroids of the two principal emission peaks, shown in the panel on the upper right of the figure, differ by only a few  $\text{km s}^{-1}$ .

The longer-integration  $2^{\circ}$  cross-cut, shown in the lower left panel of Fig. 7, sliced the object at declination  $7^{\circ}54'$ , approximately through the central location of the feature. The  $\alpha, v_{\text{LSR}}$  slice shows both the strong asymmetry of the high  $N_{\text{HI}}$  core as well as the much more symmetric halo in which the core is embedded. The object as a whole displays a kinematic gradient, spanning  $v_{\text{LSR}}$  from  $-102 \text{ km s}^{-1}$  to  $-110 \text{ km s}^{-1}$ .

The lopsided nature of the high  $N_{\text{HI}}$  core in this CHVC is evident in the upper right panel of Fig. 12, showing the edge profiles. The Eastern edge of the core is poorly resolved at the  $3'.5$  resolution of the Arecibo data. However, it is remarkable that the low  $N_{\text{HI}}$  envelope of this core (below about  $10^{18.2} \text{ cm}^{-2}$ ) shows a high degree of symmetry. The kinematic structure, shown in the upper right of Fig. 14, is well fit by a single Gaussian, with FWHM of  $22 \text{ km s}^{-1}$ . The object is clearly defined against its spatial and kinematic background, and so could be measured to column depths as low as  $10^{17.5} \text{ cm}^{-2}$ .

### 5.8. CHVC 202+30+057

CHVC 202+30+057 is one of the first objects encountered at positive LSR velocities, as longitudes increase beyond that of the Galactic anticenter. It is found in the general  $(l, b, v_{\text{LSR}})$  region populated by the anomalous-velocity features studied first by Wannier & Wrixon (1972) and Wannier et al. (1972). The two-dimensional shallow Arecibo image in the upper left of Fig. 8 shows a rather simple elongated structure, blending with HI emission from the conventional Milky Way disk at the higher declinations.

The declination chosen for the deep  $2^\circ$  cross-cut,  $21^\circ 46'$ , slices the peak  $N_{\text{HI}}$  concentration. The  $\alpha, v_{\text{LSR}}$  slice shows that the principal core can be adequately separated from Milky Way contamination. The feature is quite broad, with a velocity FWHM of about  $25 \text{ km s}^{-1}$ , and little gradient over the region contributing most of the emission.

The  $N_{\text{HI}}$  profile for this object, plotted on the lower left of Fig. 12, reaches column densities below  $10^{18} \text{ cm}^{-2}$  toward the East, but the spatial coverage to the West is insufficient to delineate the true source extent. The kinematic behavior shown in Fig. 14 is rather straightforward. Although the single-Gaussian fit leaves a substantial residual on the low-velocity wing, it is not clear if this residual is due to contamination by gas in the disk of the Milky Way rather than to a broad halo of diffuse gas in the CHVC.

### 5.9. CHVC 204+30+075

CHVC 204+30+075 was cataloged by BB99 and subsequently was one of the six CHVCs imaged with the Westerbork Synthesis Radio Telescope by BB00. In the data from the Dwingeloo 25-m telescope the object is quite intense, with a peak temperature of 1.19 K, and the largest LDS flux,  $305 \text{ Jy km s}^{-1}$ , of any of the cataloged CHVCs. The Arecibo two-dimensional mapping is shown in the upper left of Fig. 9: for this target, the Nyquist-sampled grid was extended in size to  $1.5^\circ \times 1^\circ$  in order to accommodate essentially the entire CHVC within the boundaries of the accessible emission. (Note that the two contours near  $(08^{\text{h}}26^{\text{m}}, 20^\circ 10')$  are a local minimum in  $N_{\text{HI}}$ .) The Arecibo image shows two principal cores, in a common envelope. The distribution of the intensity-weighted velocity centroids shown in the panel on the upper right of Fig. 9 shows substantial structure, with the Northern core showing a particularly pronounced kinematic gradient.

The constant-declination deep-integration slice sampled a strip along  $\delta = 20^\circ 1' 30''$ . The HI data on the strip allow tracking of the Eastern edge of the object down to about  $N_{\text{HI}} = 10^{18} \text{ cm}^{-2}$ , but the spatial coverage was not sufficient to delineate the Western edge beyond  $N_{\text{HI}} = 10^{19.4} \text{ cm}^{-2}$ .

The spatial and kinematic cuts through the centroid of this CHVC are shown in the panels on the lower right

of Figs. 12 and 14, respectively. The Eastern  $N_{\text{HI}}$  profile is only marginally resolved with the  $3.5$  Arecibo beam. A single Gaussian of FWHM  $26 \text{ km s}^{-1}$  accounts for the spectral cross-cut through the centroid.

### 5.10. CHVC 230+61+165

CHVC 230+61+165 was cataloged by BB99 and was also one of the six CHVCs imaged with the WSRT by BB00. The primitive map of this object shown by BB99 was based on LDS data sampled on a  $0.5$  lattice; on such a coarse grid the core was essentially unresolved, but the map did show a hint of some surrounding emission. The shallow Nyquist-sampled Arecibo image shown in the upper left of Fig. 10 reveals several resolved cores, clearly embedded in a common envelope. The panel on the upper right shows that the several cores are each characterized by a somewhat different velocity centroid.

The longer-integration  $\alpha, v_{\text{LSR}}$  slice shown at the lower left of Fig. 10 was made along declination  $15^\circ 28'$ , a direction crossing the CHVC near the centroid of the emission from the object as a whole, but passing through one of the minor cores. The position, velocity map shows a knot of emission, centered near  $156 \text{ km s}^{-1}$ , with little variation in either centroid velocity or in velocity FWHM.

The panels on the lower right of Figs. 11 and 13 show the spatial and kinematic cross sections, respectively, through the centroid of the emission sampled in the longer-integration slice. Although the halo may be detected below  $N_{\text{HI}} = 10^{18} \text{ cm}^{-2}$  further to the East than the West this is very near the noise floor for this field. The single-Gaussian fit, although roughly adequate in shape, leaves residuals above the noise level which are suggestive of unresolved detailed structure.

## 6. Insights based on comparison of the Arecibo and WSRT results for two CHVCs

It is instructive to compare the properties of CHVCs revealed by the Arecibo filled-aperture telescope with those revealed by the Westerbork synthesis instrument. We anticipate in this section the general conclusion that neither a large filled-aperture antenna such as the Arecibo one nor a synthesis instrument such as the WSRT will, alone, suffice to reveal the details of the core/halo morphology which pertains to the CHVCs. The picture which has emerged from the total of eight CHVCs imaged with the WSRT by Wakker & Schwarz (1991) and by BB00 is that of compact cores with angular sizes typically of a few arcmin. The HI linewidths of the cores are rather narrow (usually less than  $10 \text{ km s}^{-1}$  FWHM) and they often display significant velocity gradients along the long dimension of an elliptical extent. At resolutions coarser than the angular size of the cores, such cores will, of course, remain unresolved.

CHVC 204+30+075 and CHVC 230+61+165 have now been observed at both the WSRT and at Arecibo. The

CNM cores of these objects were imaged by BB00 using the WSRT at 28 arcsec angular resolution; the 3.5-arcmin resolution of the Arecibo data is insufficient to resolve the cold knots. On the other hand, the interferometer does not detect the diffuse halos which so clearly envelop the objects studied in the Arecibo data. More important is the complete change of character of the H I line profiles when full sensitivity to the diffuse halos is present, as in the Arecibo total-power data presented here. As seen in the figures, as well as in Table 2, most lines-of-sight are dominated by the emission from the diffuse halos, leading to much broader total H I linewidths of about  $25 \text{ km s}^{-1}$  FWHM. The velocity gradients of individual cores are diluted by this background contribution to such an extent that they can often not even be discerned.

The left-hand panel of Fig. 15 shows the H I column density distribution in CHVC 204+30+075 derived from the WSRT data at an angular resolution of 1 arcmin (from BB00) overlaid on the Arecibo data. Effectively none of the diffuse emission is detected in the WSRT data. Consequently, the velocity field and spectra shown in Fig. 8 of BB00 are dramatically different from those shown in Fig. 9. To affirm that the WSRT  $N_{\text{HI}}$  results are compatible with those from Arecibo requires the realization that the WSRT has not responded to the diffuse halo prominently seen enveloping the cores in the Arecibo data, whereas the Arecibo angular resolution has not been sufficient to reveal the core details. The comparison of the column density distribution of H I in CHVC 230+61+165 made with the WSRT and Arecibo telescopes, shown in the right-hand panel of Fig. 15, leads to similar conclusions. Only the compact CNM cores, with their narrow emission lines, are detected in the synthesis data; the total power data, on the other hand, are completely dominated by the diffuse, broader-line-width, WNM halos.

This same effect has substantial implications for the interpretation of H I observations of some nearby spiral galaxies. Dickey et al. (1990) and Rownd et al. (1994) have measured the radial distribution of H I linewidths in the galaxies NGC 1068 and NGC 5474 from VLA imaging data, and quote velocity dispersions as low as  $6 \text{ km s}^{-1}$  (or  $14 \text{ km s}^{-1}$  FWHM) in the outer disks of these systems (at  $N_{\text{HI}} \sim 10^{20} \text{ cm}^{-2}$ ). However, the VLA observations only detected about half of the total H I flux in these galaxies. It is clear that the missing flux is in a smoothly distributed component — hence its non-detection in the synthesis data — and quite likely that it represents a WNM component with the broader intrinsic linewidth (of about  $25 \text{ km s}^{-1}$  FWHM) we have measured here. This conjecture is supported by the Arecibo observations of M33 of Corbelli et al. (1989), who consistently find H I linewidths of about  $25 \text{ km s}^{-1}$  FWHM (whenever the signal-to-noise ratio was adequate) at the largest detected radii of that galaxy. The generality of this conclusion depends, of course, on the match of interferometer sensitivity to diffuse structures in the specific object under study. From our resolved detection of the warm halos in the Arecibo data we can make concrete estimates of the

required brightness sensitivity. Peak brightnesses of the WNM halos seen in Figs. 1–10 are between 20 and 50 mK over about  $20 \text{ km s}^{-1}$ . Direct WNM detection therefore requires a brightness temperature RMS,  $dT_B < 10 \text{ mK}$  over  $20 \text{ km s}^{-1}$  for emission that fills the beam. For comparison, a 12 hour integration with the VLA D configuration provides a theoretical RMS of 60 mK over  $20 \text{ km s}^{-1}$  in a naturally weighted image (Perley 2000) for which the beamsize is about 65 arcsec FWHM. If a physical resolution of 3 kpc were required, this beamsize would suffice out to a distance of 10 Mpc. However, the 60 mK RMS of a 12 hour observation would only ever allow detection of the CNM peaks and the very brightest portions of an underlying WNM.

The WSRT data have indicated that the CHVC cores do not have an intrinsically Gaussian spatial or kinematic form, either when viewed individually or as an ensemble of several cores within one CHVC halo. The accuracy of a single-Gaussian fit to the Arecibo cross-cuts is not at odds with this conclusion, if one recognizes that it is predominantly the flux from the halo which is being fit. If the cross-cut emission were being contributed by a collection of narrow-line-width CNM cores, kinematically spanning some  $20 \text{ km s}^{-1}$ , then the cross-cut spectra would be characterized by the same FWHM as has been observed, but the wings of the spectrum would be steep; in fact, the spectral wings are consistent with WNM linewidths.

Furthermore, the conclusion which we have been able to draw from the Arecibo observations reported here, namely that the column depths in the outer regions of the CHVCs fall off as an exponential with radius, implies that for sensitivity-limited data, both the measured sizes and fluxes will depend on the sensitivity and resolution employed. (We note in this regard that it is reasonable to expect that observations, made with currently available instrumental parameters, of any analogous objects which might be located beyond the Local Group would be severely sensitivity limited.) To illustrate this point with a concrete example, we have plotted the cumulated fractional flux as function of radius in Fig. 11 for CHVC 158–39–285, assuming that the measured radial profile for this object has azimuthal symmetry. Resolved observations of this object (with an angular resolution at least as good as 500 arcsec) with a limiting column density sensitivity of  $\sim 10^{19} \text{ cm}^{-2}$  would measure a source radius of about 1000 arcsec and only detect some 50% of the total flux density. Only with a resolved column density sensitivity of  $\sim 10^{18} \text{ cm}^{-2}$  or better would more than 90% of the flux density be recovered. If the source is not well-resolved by the telescope beam, then the total flux per beam must be evaluated and compared with the mass sensitivity of the observation over the typical total source linewidth. These considerations are crucial in assessing the detectability of a population of CHVCs when viewed at large distances.

## 7. Source symmetries and asymmetries

The sensitive, high-resolution cross-cuts described in §5 provide the opportunity for studying the edge profiles of each source in our sample down to very low column densities as well as their degree of reflection-symmetry. Since only a single positional angle (along a line of constant declination) has been observed to this depth in each source we are very sensitive to the particular sub-structures we happen to encounter. If instead we were able to employ azimuthal averaging from a fully-sampled large-area map, we would expect such sub-structures to average away to a large extent. Nonetheless, some trends are worthy of discussion on the basis of this limited source sampling.

Firstly, the high column density regions ( $N_{\text{HI}} > 10^{18.5} \text{cm}^{-2}$ ) of each source, which we term cores, show a high degree of structure. Typically, several of such cores are found in each source, but even if there is only one prominent core component it is not necessarily accurately centered within the diffuse low column density halo. Prominent cores which we sample that are substantially off-center are seen in CHVC 100–49–383, CHVC 148–32–144 and CHVC 204+30+075. In these cases, the two degree scan length of our deep cross-cut does not extend to both edges of the source, making it impossible to comment on the degree of symmetry seen in the underlying halo component. Even in less extreme cases, our spatial coverage is sometimes insufficient to extend beyond the range of detectable emission on at least one side of the source, so that comparisons can only be made over a limited range of column densities.

The comparison of the “East” and “West”  $N_{\text{HI}}$  profiles in Figs.11–12 is shown for the range of column densities that is above the noise floor ( $> 2\sigma$ ) in each case. The origin of the “radius” axis in these figures was arbitrarily chosen to correspond to the location of peak column density along the single cross-cut. Positive or negative shifts in position are therefore allowed, and source symmetry should be judged on the basis of agreement in the local slope of the two profiles rather than on their “radial” position. With these caveats in mind, it becomes clear that substantial asymmetries appear to be confined to the regions of moderately high column density ( $N_{\text{HI}} > 10^{18.5} \text{cm}^{-2}$ ), while below this column density a high degree of reflection-symmetry is present in all cases. Even those sources that have extreme asymmetries at  $N_{\text{HI}} > 10^{19} \text{cm}^{-2}$ , like CHVC 186–31–206 and CHVC 198–12–103, have effectively identical edge profiles below  $N_{\text{HI}} > 10^{18.2} \text{cm}^{-2}$ .

The large disparity in source symmetry at high and low  $N_{\text{HI}}$  seen in some sources, particularly in CHVC 198–12–103, has important implications for the physical conditions in and around these sources. While substantial asymmetry of the high  $N_{\text{HI}}$  regions might be interpreted as implying an externally induced ram pressure origin (eg. Brüns et al. (2000), this seems to be ruled out by the high degree of symmetry seen in the low  $N_{\text{HI}}$  envelopes. If the core asymmetries were due to such an external influence, then the asymmetries should be even

more severe in the diffuse halos, which clearly is not the case.

Significant asymmetries at high column density levels are also commonly observed in external galaxies. Richter & Sancisi (1994) concluded that at least 50% of all spiral galaxies have strong or mild asymmetries based on analysis of their integrated H I line profiles. Swaters (1999) extended this analysis with the assessment of asymmetry in a sample of 73 late-type dwarf galaxies. He finds strong asymmetries in 34% of his sample and weak asymmetries in a further 16%. The incidence of significant asymmetry at high  $N_{\text{HI}}$  in our sample of CHVCs is about 6 out of 10 based on our limited spatial sampling. This is quite comparable to the rate of incidence seen in nearby galaxies.

## 8. 3-D morphology and distance

The reflection-symmetry of CHVC edge profiles at low column densities together with the roughly circular appearance of each source at low angular resolution ( $\sim 30$  arcmin) imply that the diffuse halo component may have a substantial degree of spherical symmetry. These properties suggest a method to constrain the three-dimensional morphology and possible distances of these objects. If we consider an intrinsically exponential distribution of atomic volume density in the diffuse WNM halos of the CHVCs with spherical symmetry of the form

$$n_{\text{H}}(r) = n_0 e^{-r/h_B} \quad (1)$$

in terms of the radial distance,  $r$ , and exponential scale length,  $h_B$ , it is possible to calculate the corresponding projected distribution of H I column density,

$$N_{\text{HI}}(r) = 2h_B n_0 \left[ \frac{r}{h} K_1 \left( \frac{r}{h_B} \right) \right], \quad (2)$$

where  $K_1$  is the modified Bessel function of order 1. This result follows from the related calculation of the edge-on appearance of an exponential stellar disk by Van der Kruit & Searle (1981).

The projected distribution of  $N_{\text{HI}}$  given by eqn. 2 is approximately exponential beyond a few scale-lengths, but flattens significantly toward small radii. The correspondence between these Bessel function scaleheights,  $h_B$ , and the most similar 1-D exponential scaleheights,  $h_e$ , (over the interval  $3h_B < r < 6h_B$ ) is about  $h_e = 1.1 h_B$ .  $N_{\text{HI}}$  profiles of the form given by eqn.2 have been overlaid on the data shown in Figs. 11 and 12. Profiles of this type provide a reasonably good description of the observed profiles and allow accurate assessment of the total atomic column density,  $N_{\text{HI}}(0)$ , and intrinsic scale-length,  $h_B$ , of the WNM halos under the assumption of crude spherical symmetry. Even in those cases where there is some asymmetry between the Eastern and Western halves of the profile at high  $N_{\text{HI}}$ , the peak  $N_{\text{HI}}$  value of the halo and the scale-length at large radii are well-defined. Due to the large offset of the bright core location from the centroid of the underlying halo in CHVC 100–49–383,

CHVC 148–32–144, and CHVC 204+30+075 only one of the edge profiles was observed in our cross-cut. However, even for these sources, the well-sampled edge of the source shows good correspondence with profiles of this form. For the sources CHVC 092–39–367, CHVC 202+30+057, and CHVC 204+30+075, the calculated  $N_{\text{HI}}$  profiles were given a linear offset from the origin in radius, since the transition from cool cores to warm halos was significantly offset from the direction that displayed the peak column density. The displayed values of the total atomic column density,  $N_{\text{HI}}(0)$ , and scale-length,  $h_B$ , are listed in Table 2 for the seven sources in which both Eastern and Western edge profiles were sampled. Significantly worse correspondence of the profiles with the data is found for variations of 0.1 dex in  $\log(N_{\text{HI}})$  and 50 arcsec in  $h$ . We find mean values of  $N_{\text{HI}}(0) = 4.1 \pm 3.2 \times 10^{19} \text{ cm}^{-2}$  and  $h = 420 \pm 90$  arcsec averaged over the 7 tabulated objects.

BB00 considered the physical conditions necessary for the shielding and condensation of CNM cores within WNM halos. While thermal pressures,  $P/k$ , of  $\sim 2000 \text{ cm}^{-3} \text{ K}$  are found in the local mid-plane of the Galaxy, these are expected to decline dramatically with height (and Galactocentric radius), falling to values below about  $100 \text{ cm}^{-3} \text{ K}$  beyond about 20 kpc (Wolfire et al. 1995). The calculations presented in Wolfire et al. suggest that for a wide range of physical conditions (metal abundance, radiation field and dust content) the transition from a two phase ISM to a WNM should occur near a thermal pressure of  $P/k \sim 100 \text{ cm}^{-3} \text{ K}$ . Only in the case of effectively primordial metal abundance is a large departure expected from this nominal transition pressure, in the sense of a much higher required thermal pressure. From the ubiquitous detection of metal line systems in quasar absorption line studies as well as a metallicity estimate for CHVC125+41–207 (BB00) it seems likely that a metal abundance of about 0.1 solar is appropriate for the CHVCs. Assuming a nominal thermal pressure of the core/halo interface in CHVCs allows calculation of the central volume density,  $n_o$ , since the kinetic temperature is known from the observed linewidths to be  $T_k = 10^4 \text{ K}$ . The distance of each object with a measured edge profile can then be estimated by assuming an equal extent in the plane of the sky and along the line-of-sight from,

$$D = \frac{N_{\text{HI}}(0)}{2hn_o} = \frac{N_{\text{HI}}(0)kT}{2hP}, \quad (3)$$

or

$$D = 335 \left( \frac{N_{\text{HI}}(0)}{10^{19} \text{ cm}^{-2}} \right) \left( \frac{P/k}{100 \text{ cm}^{-3} \text{ K}} \right)^{-1} \left( \frac{h}{100''} \right)^{-1} \text{ kpc}. \quad (4)$$

These estimated distances are listed in Table 2 and vary between 150 and 850 kpc, with a mean of  $400 \pm 280$  kpc.

A similar method of distance estimation for HVCs was suggested by Ferrara & Field (1994), although in their treatment a uniform volume density of the gas was assumed, which complicates the identification of the angular size that should be related to the line-of-sight depth. The distances to several of the diffuse HVC complexes have

been found, using more direct methods (e.g. van Woerden et al. 1999), to lie in the range of several to several tens of kpc. But the distinctions between the diffuse HVC complexes and the population of compact, isolated CHVCs are sufficiently robust, and the distance parameter so crucial, that investigations of alternative measures of distance are required. We note that the WSRT interferometric imaging carried out by Wakker & Schwarz (1991) towards two CHVCs and along representative lines-of-sight towards four HVC complexes revealed that the two object classes have very different properties. A much larger fraction of the object flux was recovered in the WSRT imaging of the CHVCs and the detected cool cores are much more subject to beam dilution effects when observed with a coarser beam. Both of these properties led Wakker & Schwarz to conclude that the CHVCs were significantly more distant than the HVC complexes.

It is important to stress that we have considered only the distribution of the observed atomic gas density in our analysis. It is likely that the edges of the atomic distribution are accompanied by an increasing proportion of ionized gas due to photoionization by external radiation. For this reason, the total gas density (the sum of atomic and ionized components) will probably be significantly shallower than the distributions shown here. However, the method of distance estimation discussed above is not effected in a systematic way by considering only the atomic rather than the total gas distribution. We only assume an approximate spherical symmetry of the atomic component, which is still expected to be the case.

We can calibrate the edge-profile method of distance determination by direct comparison with the observed edge-profiles of low mass galaxies. A comprehensive study of 73 late-type dwarf galaxies based on a uniform database has recently been presented by Swaters (1999). Optical and H I properties, including the exponential scale-lengths of H I in the outer disks are derived for this entire sample. We have taken all of the well-resolved, high signal-to-noise data for the lowest mass systems studied by Swaters by selecting the galaxies nearer than 10 Mpc, with line profile half-widths ( $W_{50}$ ) less than  $100 \text{ km s}^{-1}$ , and average H I surface density within 3.2 optical disk scale-lengths ( $< \Sigma_{\text{HI}} >_{3.2h}$ ) greater than  $2.5 M_{\odot} \text{ pc}^{-2}$ . The exponential scale-length fit to the outer disk H I for the 15 selected galaxies is plotted against the line profile half-width in the left-hand panel of Fig. 16. There is only modest variation in the outer disk scale-lengths and no apparent variation with profile line-width. The mean outer disk scale-length is  $h_e = 11.7 \pm 4.4$  kpc. If we adopt this mean outer disk scale-length as a constant for all low mass galaxies and calculate the corresponding distances implied by  $h_e$  in angular units, we recover the accepted galaxy distances to better than a factor of two, as shown in the right-hand panel of Fig. 16. The corresponding value of  $h_B$  for a Bessel function scale-length is  $h_B = 10.6 \pm 4.0$  kpc. Applying this same yard-stick to our measurements of halo scale-length in the CHVCs yields the distance estimates in the last column of Table 2. The derived distances

vary between 320 and 730 kpc, with a mean of  $500 \pm 130$  kpc, and show agreement to within about a factor of two with our estimates from eqn. 4.

## 9. Discussion and conclusions

The Arecibo imaging reported here has demonstrated that a nested core/halo geometry is characteristic of the targeted CHVCs, and allows the direct resolved detection of the halo component for the first time in these compact objects. The compact cores identified in our earlier WSRT interferometric data were only marginally resolved at angular resolutions of  $2'$  or less; such cores would remain severely unresolved in the Arecibo beam. On the other hand, the signal from diffuse halo material is effectively undetected in the synthesis data and can only be studied by deep total-power imaging.

The measured FWHM linewidths in the halos are typically in the range 20 to  $25 \text{ km s}^{-1}$ . The various circumstances, in particular blending, which would render this measure an upper limit to the thermal broadening are shown to be not especially important by the accuracy of the single-Gaussian spectral fits, particularly in the wings of the spectra. The residuals of the single-Gaussian fits are in some cases in excess of the RMS noise of some 10 mK at a velocity resolution of  $1 \text{ km s}^{-1}$ . However, the dimples evident in the profiles imply unresolved structure in the ensemble of cores. The general shape of the profile, and particularly the form of the spectral wings, is consistent with thermal emission from H I at a kinetic temperature near  $10^4 \text{ K}$ . Thus these observations provide evidence that the halos of the CHVCs observed are comprised of gas in the WNM phase, hypothesized as providing the neutral shielding column required if the CNM cores are to remain stable in the presence of an ionizing radiation field.

A kinematic gradient aligned with the elongation of the object was observed in several CHVC cores, most notably in CHVC 158–39–285 and CHVC 186–31–206. Since the long-integration Arecibo data was limited to a single East–West cross-cut that only rarely coincides with the direction of elongation, this conclusion can not be stated firmly for all of the objects observed. The kinematic gradients are compatible with the expectation of slow rotation in a flattened disk system, and are consistent with the modeling which BB00 applied to two well-resolved cores in CHVC 204+30+075, showing that these cases can be described by rotation curves of Navarro et al. (1997) cold dark matter halos of mass about  $10^8 M_{\odot}$ .

The halos and the cores are evidently kinematically decoupled, in the sense that a core region may show a systematic kinematic gradient when the halo does not, but remains centered on the systemic velocity of the CHVC. CHVC 158–39–285 is a particular example of this situation (although the same effect can also be seen in CHVC 100–48–383 and CHVC 186–31–206), which is compatible with rotation but seems difficult to reconcile with an external cause for the kinematic distortion, for example by a tidal shear. An external force would be

expected to produce a more severe distortion of the diffuse envelopes than on the dense cores. A tidal shear or other externally caused distortion seems unlikely for several other reasons, including the apparent isolation of the CHVCs and the evidence for a Local Group deployment.

Substantial asymmetries characterize the high column density ( $N_{\text{HI}} > 10^{18.5} \text{ cm}^{-2}$ ) portions of the H I distributions in 6 out of 10 of the CHVCs imaged. Particularly striking examples of this high  $N_{\text{HI}}$  lopsidedness are provided by CHVC 100–49–383, CHVC 148–32–144, and CHVC 198–12–103. This rate of occurrence of asymmetry is comparable to the 50% found in large samples of nearby galaxies by Richter & Sancisi (1994) and Swaters (1999). In contrast, the low column density ( $N_{\text{HI}} < 10^{18.5} \text{ cm}^{-2}$ ) portions of the edge profiles display a very high degree of reflection-symmetry in all cases where our spatial coverage extends to these levels. Even the extreme source, CHVC 198–12–103, displays essentially identical edge profiles below  $N_{\text{HI}} = 10^{18.2} \text{ cm}^{-2}$ . The high degree of symmetry found in the low  $N_{\text{HI}}$  halos relative to the high  $N_{\text{HI}}$  cores argues against external mechanisms, like ram-pressure confinement, as the cause of the asymmetries seen in the cores.

The  $N_{\text{HI}}$  profiles of the warm halos plotted in Fig. 11 and 12 can be described well, by the sky-plane projection of a spherical exponential distribution of H I volume density. In the most sensitive cross-cuts the exponential edge profile can be tracked down to  $N_{\text{HI}} = 10^{17.5} \text{ cm}^{-2}$ . Thus, the measured size and total flux of the CHVCs will be dependent on the resolution and on the sensitivity of the observation. This point is of particular concern when considering searches for CHVC counterparts which might be associated with galaxies or groups of galaxies beyond the Local Group.

The distinctive halo profiles also allow estimation of the peak halo column density and exponential scale-length in each object. When combined with an estimate of the nominal thermal pressure at the core/halo interface, the distance to each object can be derived by assuming approximate spherical symmetry. Seven of the ten objects studied indicate distances which vary between 150 and 850 kpc, with a mean of  $400 \pm 280$  kpc. If instead we adopt the mean observed outer disk exponential scale-length of about 11 kpc found in a sample of nearby late-type dwarf galaxies, the same set of objects yield consistent distances that vary between 320 and 730 kpc with a mean of  $500 \pm 130$  kpc.

## 10. Summary

The Arecibo imaging of ten CHVCs, combined with the BB00 WSRT imaging, lead to the following conclusions:

- The compact high-velocity clouds display a core/halo morphology.
- The CNM of the cores of CHVCs are better revealed in synthesis data than in filled-aperture data because of their small angular scales.

- The WNM of the diffuse halos of CHVCs are better revealed in filled-aperture data than in synthesis data because of their diffuse morphology and large angular sizes.
- The FWHM linewidth of the CHVC halo gas is typically  $25 \text{ km s}^{-1}$ , consistent with the expected WNM thermal linewidth of  $10^4 \text{ K}$  gas.
- Some of the cores exhibit a kinematic gradient, consistent with rotation.
- The differing kinematics of the cores and the halos is consistent with the cores being kinematically decoupled from the halos.
- Since the halos do not commonly share the kinematic gradient of cores, an external origin of the gradient is unlikely.
- 60% of the CHVCs studied display significant asymmetries in the HI distribution at high column density ( $N_{\text{HI}} > 10^{18.5} \text{ cm}^{-2}$ ).
- There is a high degree of reflection-symmetry in the low column density ( $N_{\text{HI}} < 10^{18.5} \text{ cm}^{-2}$ ) edge profiles in all seven cases where the spatial coverage extends to these levels.
- The presence of a highly symmetric halo exterior to an asymmetric core argues against external mechanisms for producing the core asymmetry.
- The HI column-density profiles of the CHVC halos are consistent with the sky-plane projection of a spherical exponential distribution of HI volume density.
- Assuming a nominal thermal pressure for the CNM/WNM interface and approximate spherical symmetry of the halos, distance estimates for individual objects can be made. These lie in the range 150 to 850 kpc.
- Assuming a “standard” outer-disk scale-height for low mass self-gravitating systems (as observed in nearby dwarf galaxies) allows distance estimates in the range 320 to 730 kpc to be made.

*Acknowledgements.* We are grateful to P. Perillat for assistance during our Arecibo observing session, to T.M. Bania for communications regarding the calibration of the data, to C. Salter and E. Howell for information regarding the beamwidth and sidelobe characteristics, and to the referee, J. Kerp, for constructive comments. The Arecibo Observatory is part of the National Astronomy and Ionosphere Center, which is operated by Cornell University under a cooperative agreement with the National Science Foundation.

## References

- Bajaja E., Morras R., Pöppel W.G.L., 1987, *Pub. Astr. Inst. Czech. Ac. Sci.* 69, 237
- Blitz L., Spergel D.N., Teuben P.J., Hartmann D., Burton W.B., 1999, *ApJ* 514, 818
- Braun R., Burton W.B., 1999, *A&A* 341, 437 (BB99)
- Braun R., Burton W.B., 2000, *A&A* 354, 853 (BB00)
- Brüns C., Kerp J., Kalberla P.M.W., Mebold U., 2000, *A&A* 357, 120
- Condon J.J., Cotton W.D., Greisen E.W., Yin Q.F., Perley R.A., Taylor G.B., Broderick J.J., 1998, *AJ* 115, 1693
- Corbelli E., Schneider S.E., Salpeter E.E., 1989, *AJ* 97, 390
- Cram T.R., Giovanelli R., 1976, *A&A* 48, 39
- Dickey J.M., Hanson M.M., Helou G., 1990, *ApJ* 352, 552
- Eichler D., 1976, *ApJ* 208, 694
- Einasto J., Haud U., Jõeveer M., Kaasik A., 1976, *MNRAS* 177, 357
- Giovanelli R., 1981, *AJ* 86, 1468
- Ferrara A., Field G.B., 1994, *ApJ* 423, 665
- Hartmann D., Burton W.B., 1997, “Atlas of Galactic Neutral Hydrogen” (Cambridge: Cambridge University Press)
- Heiles C., 1999, Arecibo Observatory Technical Memo AOTM 99-02
- Helmi A., White S.D.M., de Zeeuw P.T., Zhao H.S., 1999, *Nature* 402, 53
- Howell E., private communication
- Ibata R., Gilmore G., Irwin M., 1994, *Nature* 370, 194
- Klypin A., Kravtsov A.V., Valenzuela O., Prada F., 1999, *ApJ* 522, 82
- Moore B., Ghigna S., Governato G., Lake G., Quinn T., Stadel J., Tozzi P., 1999, *ApJ* 524, L19
- Navarro J.F., Frenk C.S., White S.D.M., 1997, *ApJ* 490, 493
- Oort J.H., 1966, *Bull. Astr. Inst. Netherlands* 18, 421
- Oort J.H., 1970, *A&A* 7, 381
- Oort J.H., 1981, *A&A* 94, 359
- Perley R.A., 2000, VLA Observational Status Summary
- Putman M.E., Gibson B.K., 1999, *PASA* 16, 70
- Richter O.-G., Sancisi R., 1994, *A&A* 290, L9
- Rownd B.K., Dickey J.M., Helou G., 1994, *AJ* 108, 1638
- Swaters R.A., 1999, PhD dissertation, University of Groningen
- van der Kruit P.C., Searle L., 1981, *A&A* 95,105
- van Woerden H., Schwarz U.J., Peletier R.F., Wakker B.P., Kalberla P.M.W., 1999, *Nature* 400, 138
- Verschuur G.L., 1975, *ARA&A* 13, 257
- Wakker B.P., Schwarz U., 1991, *A&A* 250, 484
- Wakker B.P., van Woerden H., 1991, *A&A* 250, 509
- Wakker B.P., van Woerden H., 1997, *ARA&A* 35, 217
- Wannier P., Wrixon G.T., 1972, *ApJ* 173, L119
- Wannier P., Wrixon G.T., Wilson R.W., 1972, *A&A* 18, 224
- Williams D.R.W. 1973, *A&AS* 8, 505
- Wolfire M.G., McKee C.F., Hollenbach D., Tielens A.G.G.M., 1995, *ApJ* 453, 673

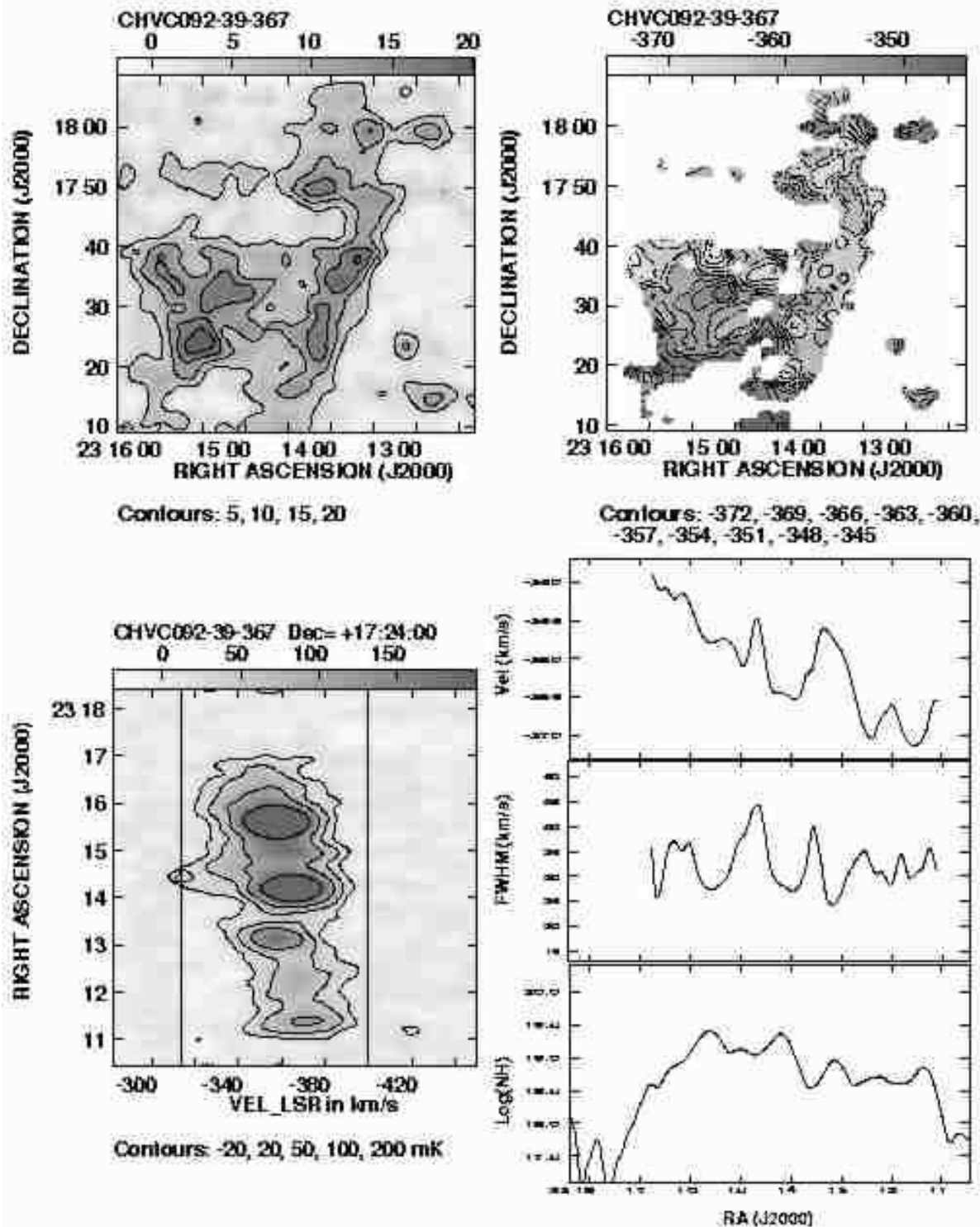


**Fig. 1.** Imaging and cross-cut data observed for CHVC 092–39–36. Upper left:  $N_{\text{HI}}$  distribution over the  $1^\circ \times 1^\circ$  grid Nyquist sampled in short integrations; the indicated contours represent units of  $10^{18} \text{ cm}^{-2}$ . The right ascension labeling refers to the tick mark above the last zero of the label. Upper right: Intensity-weighted velocity field across the mapped grid; the contours represent  $v_{\text{LSR}}$  in units of  $\text{km s}^{-1}$ . Lower left:  $\alpha, v_{\text{LSR}}$  slice sampled in longer integrations at the indicated declination; the contours represent  $T_{\text{B}}$  in units of mK. Lower right: Centroid  $v_{\text{LSR}}$ , velocity FWHM, and  $N_{\text{HI}}$  determined along the  $\alpha, v_{\text{LSR}}$  slice, within the velocity limits indicated by the vertical lines in the panel on the lower left.

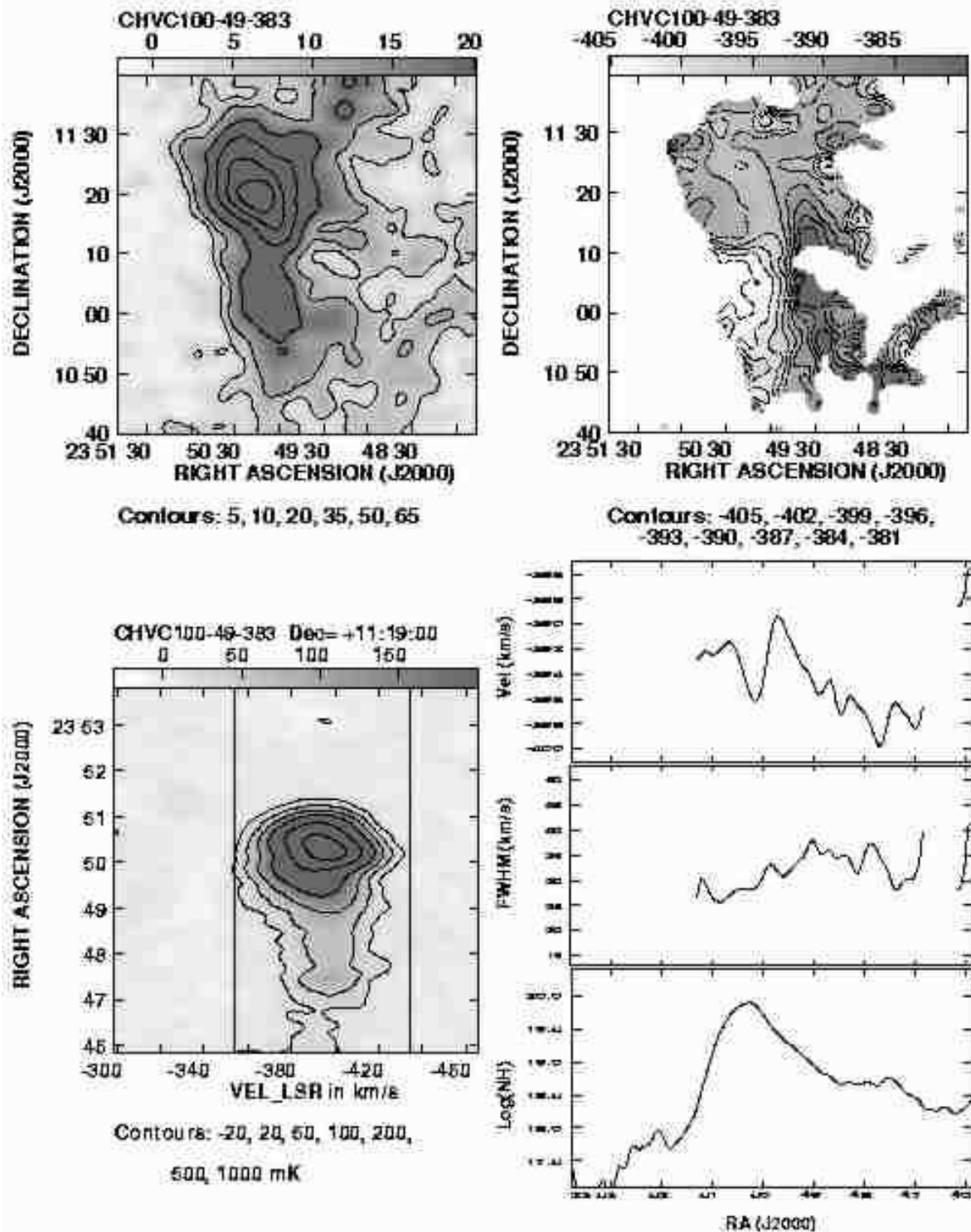


Fig. 2. Imaging and cross-cut data observed for CHVC 100–49–383 as in Fig. 1.

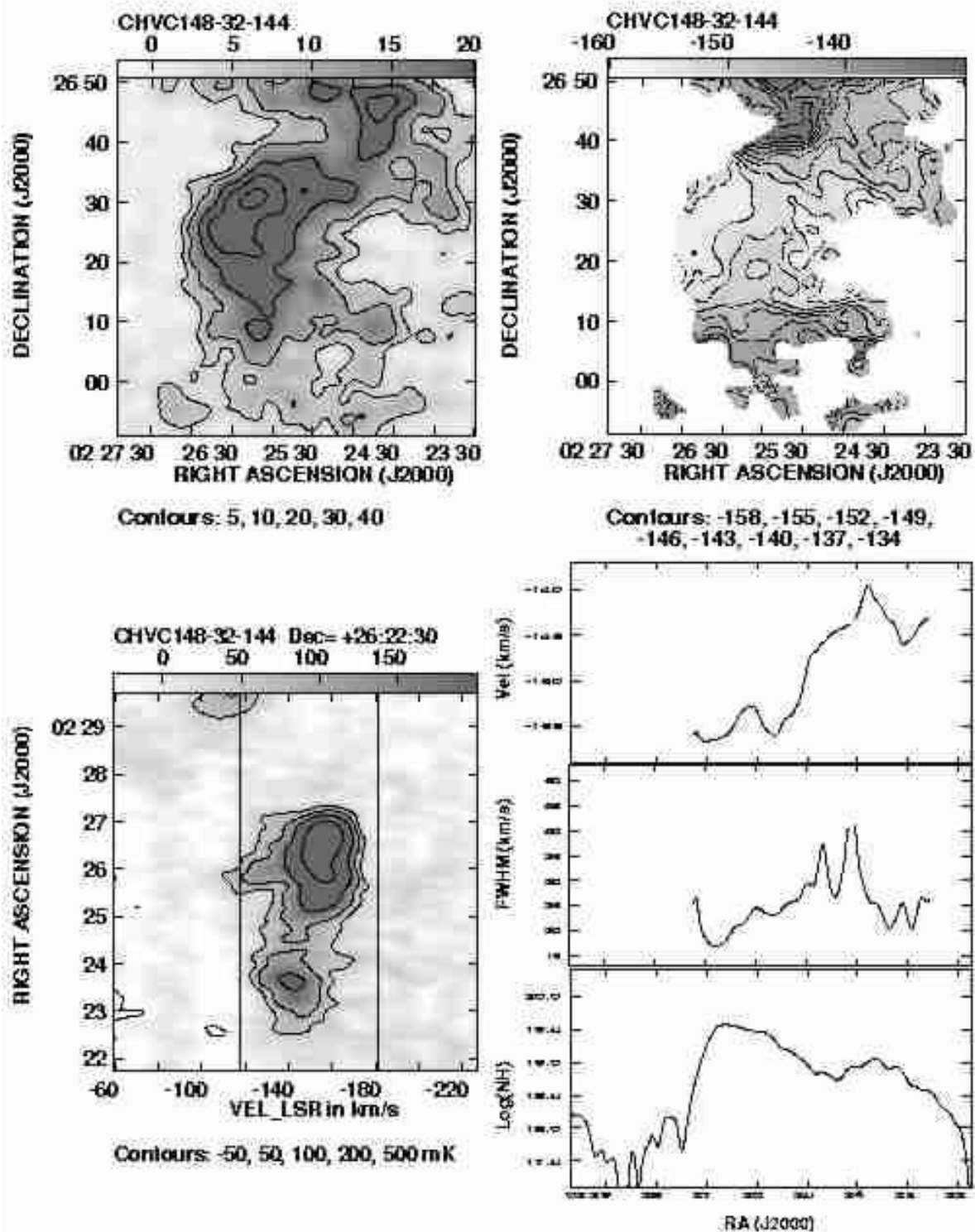


Fig. 3. Imaging and cross-cut data observed for CHVC 148–32–144 as in Fig. 1.

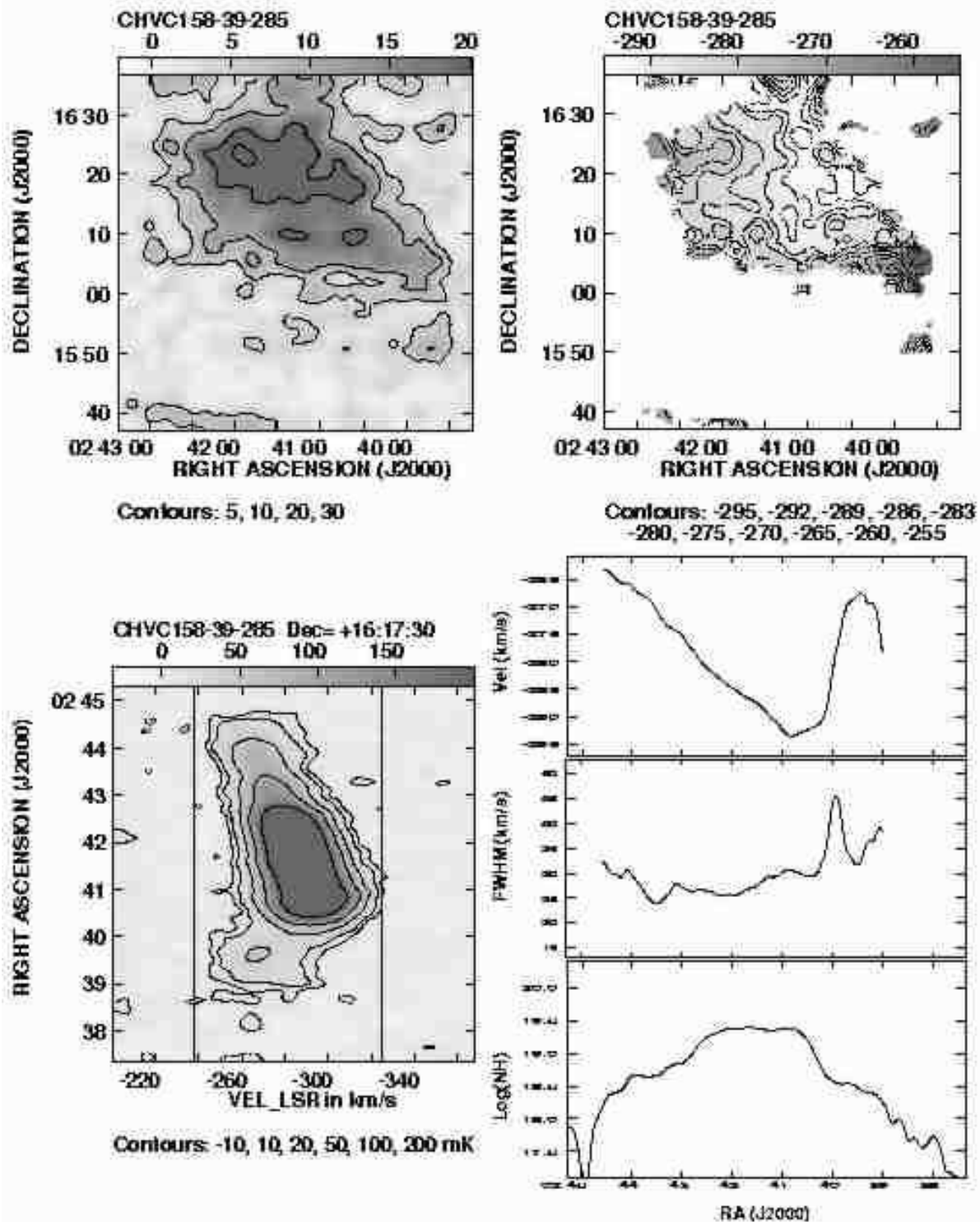


Fig. 4. Imaging and cross-cut data observed for CHVC 158–39–285 as in Fig. 1.

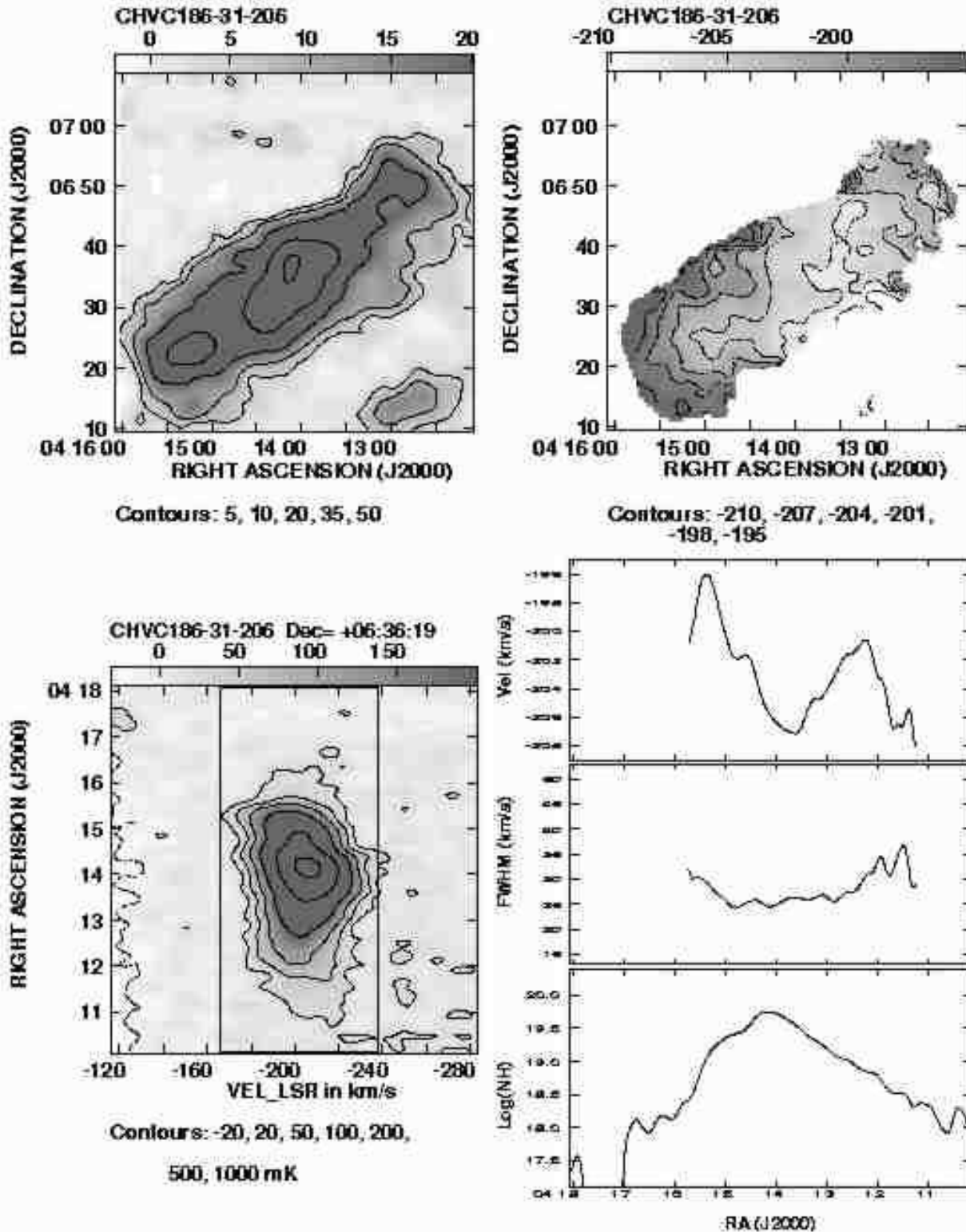


Fig. 5. Imaging and cross-cut data observed for CHVC 186–31–206 as in Fig. 1.

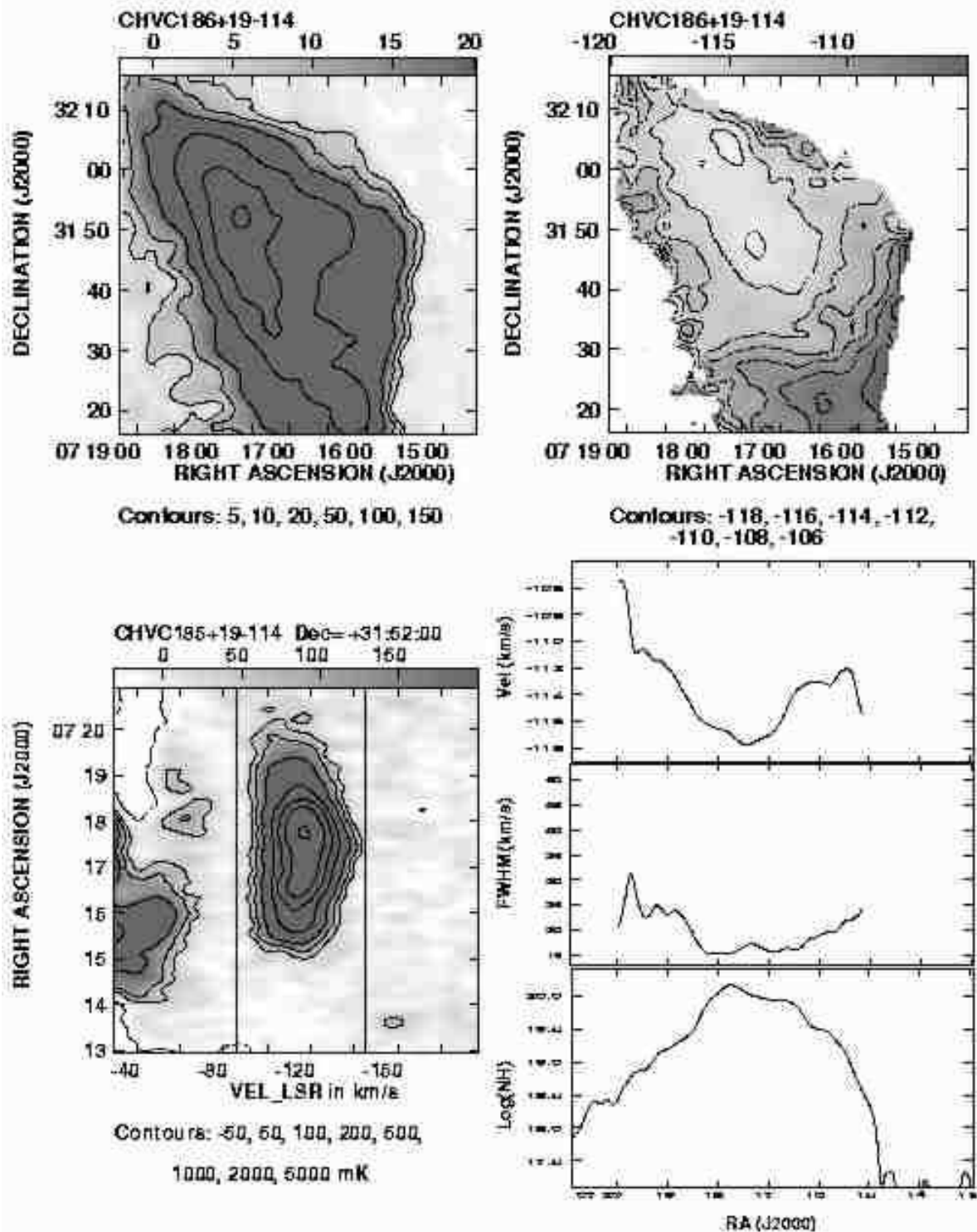
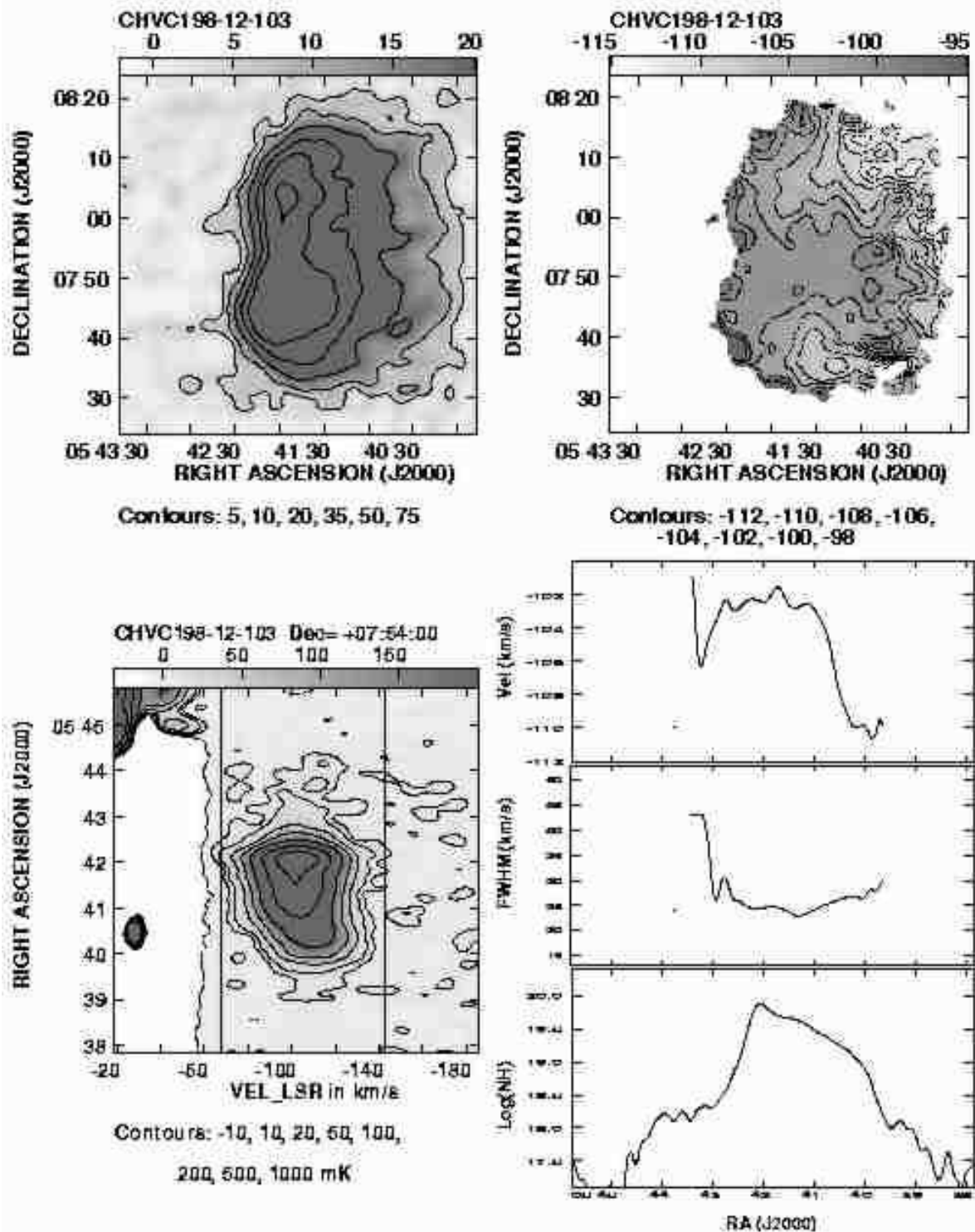


Fig. 6. Imaging and cross-cut data observed for CHVC 186+19-114 as in Fig. 1.



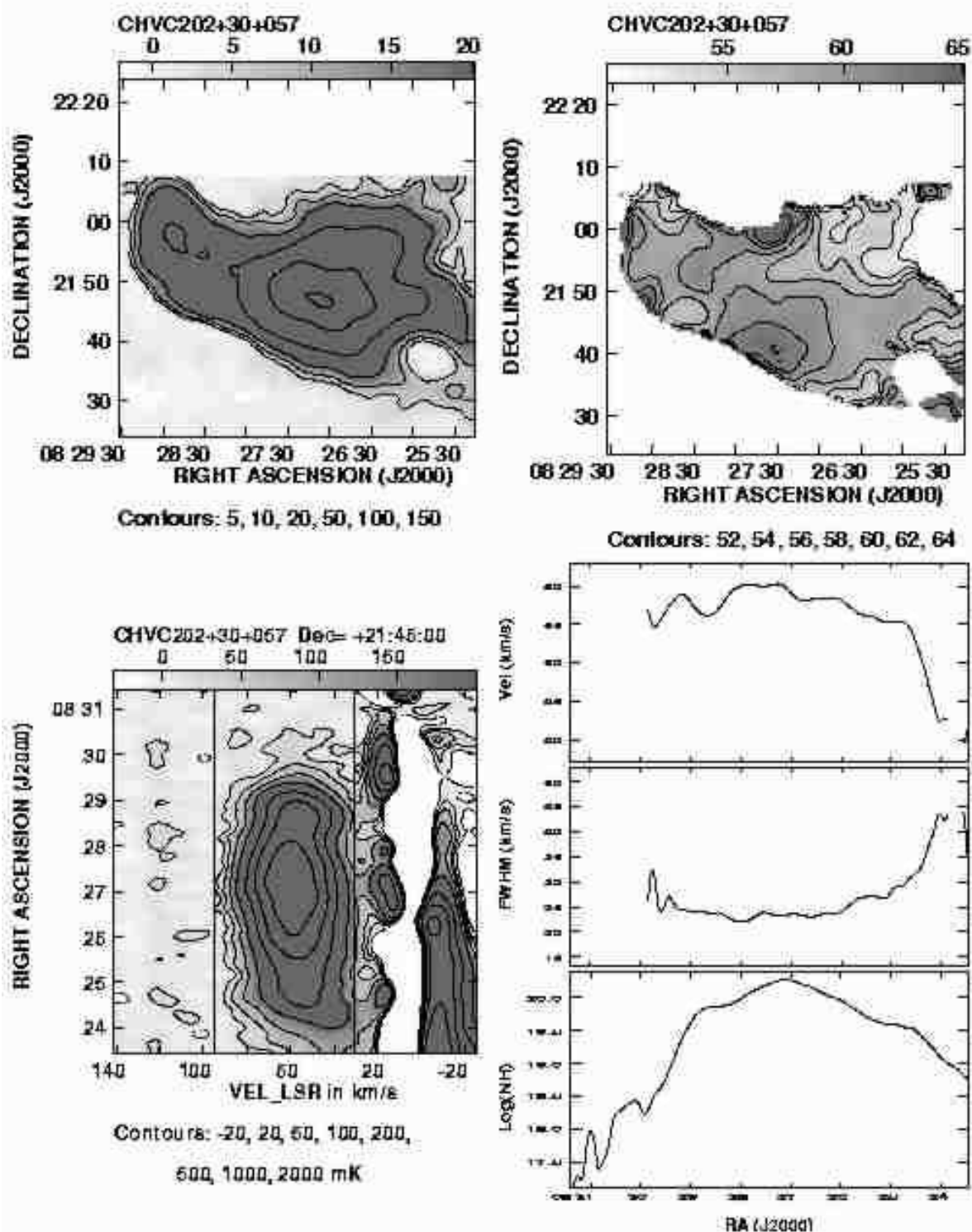


Fig. 8. Imaging and cross-cut data observed for CHVC 202+30+057 as in Fig. 1.

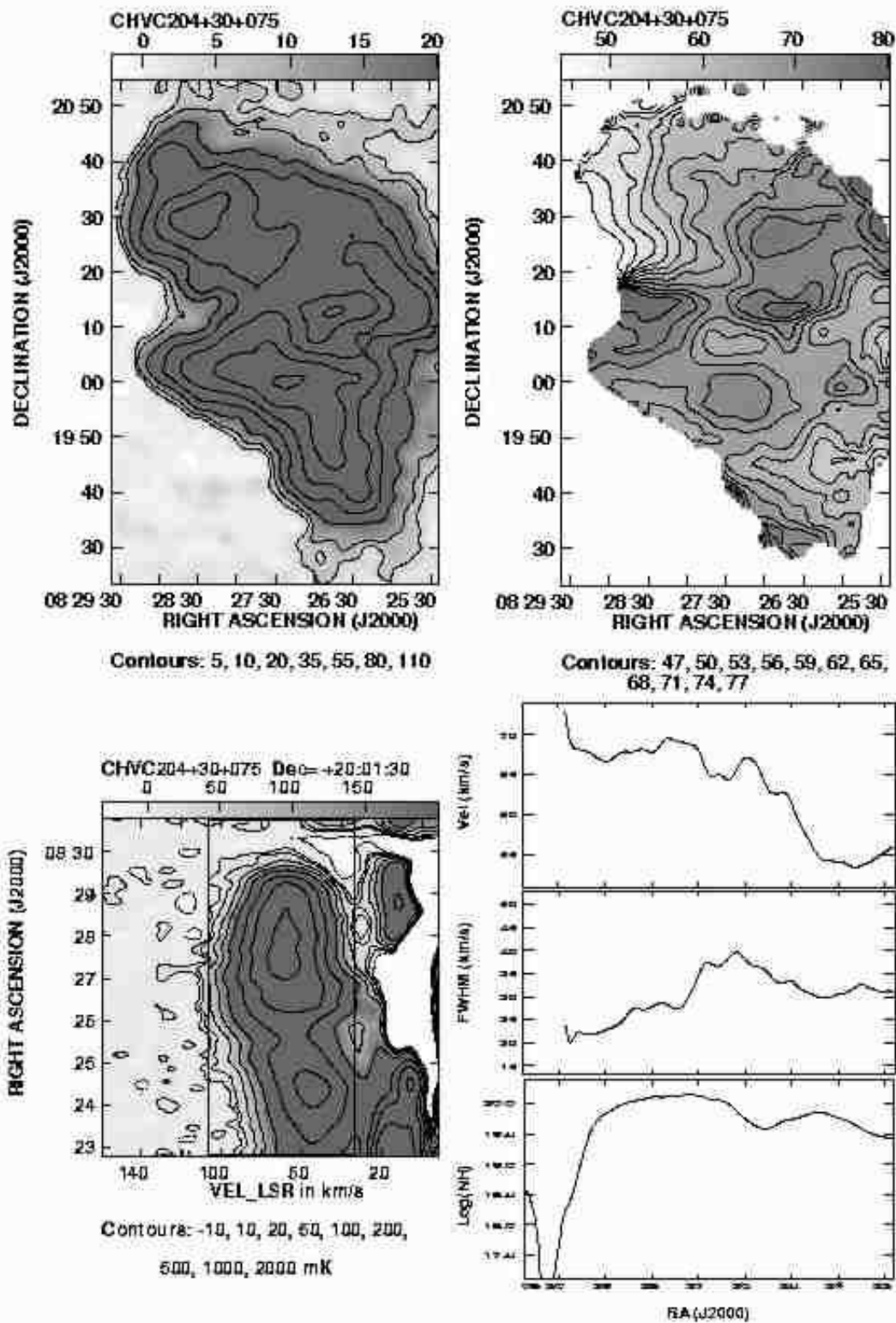
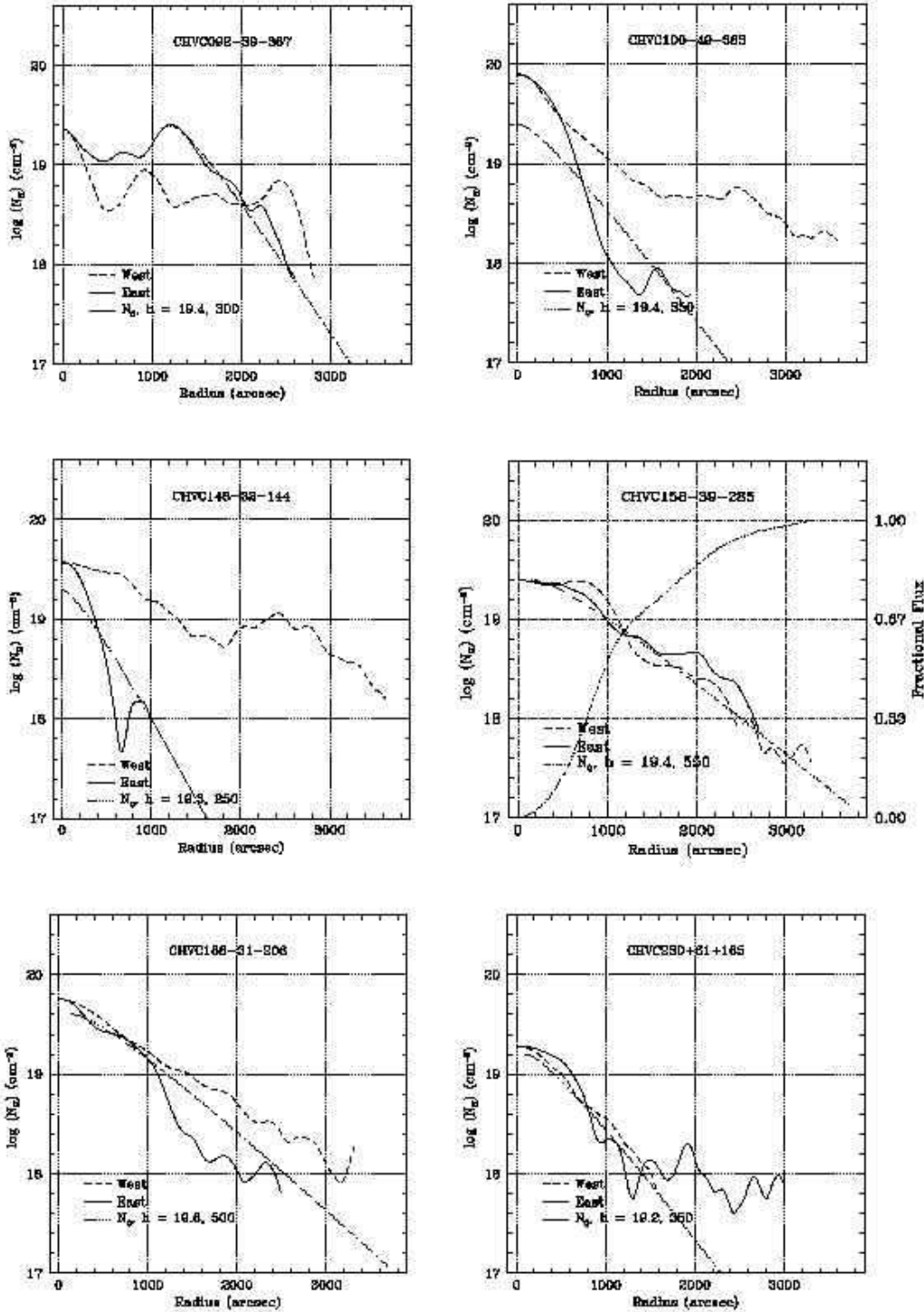


Fig. 9. Imaging and cross-cut data observed for CHVC 204+30+075 over the  $1^\circ \times 1.^\circ 5$  grid as in Fig. 1.





**Fig. 11.** Column-density profiles of the indicated CHVCs. The logarithm of HI column density is plotted against distance to the East and West of the emission peak in the lower-left panel of Figs. 1–10. The dotted curve overlaid on the observed  $\log(N_{\text{HI}})$  values corresponds to the sky-plane projection of a spherical exponential distribution of atomic volume density, with the indicated central  $\log(N_{\text{HI}})$  and scale height in arcsec. The asymmetric profiles of CHVC100–49–383 and CHVC148–32–144 show large departures from the overlaid curves. In the panel for CHVC158–39–285, the accumulated fractional flux (assuming circular source symmetry) is indicated by the increasing curve which is labeled to the right.

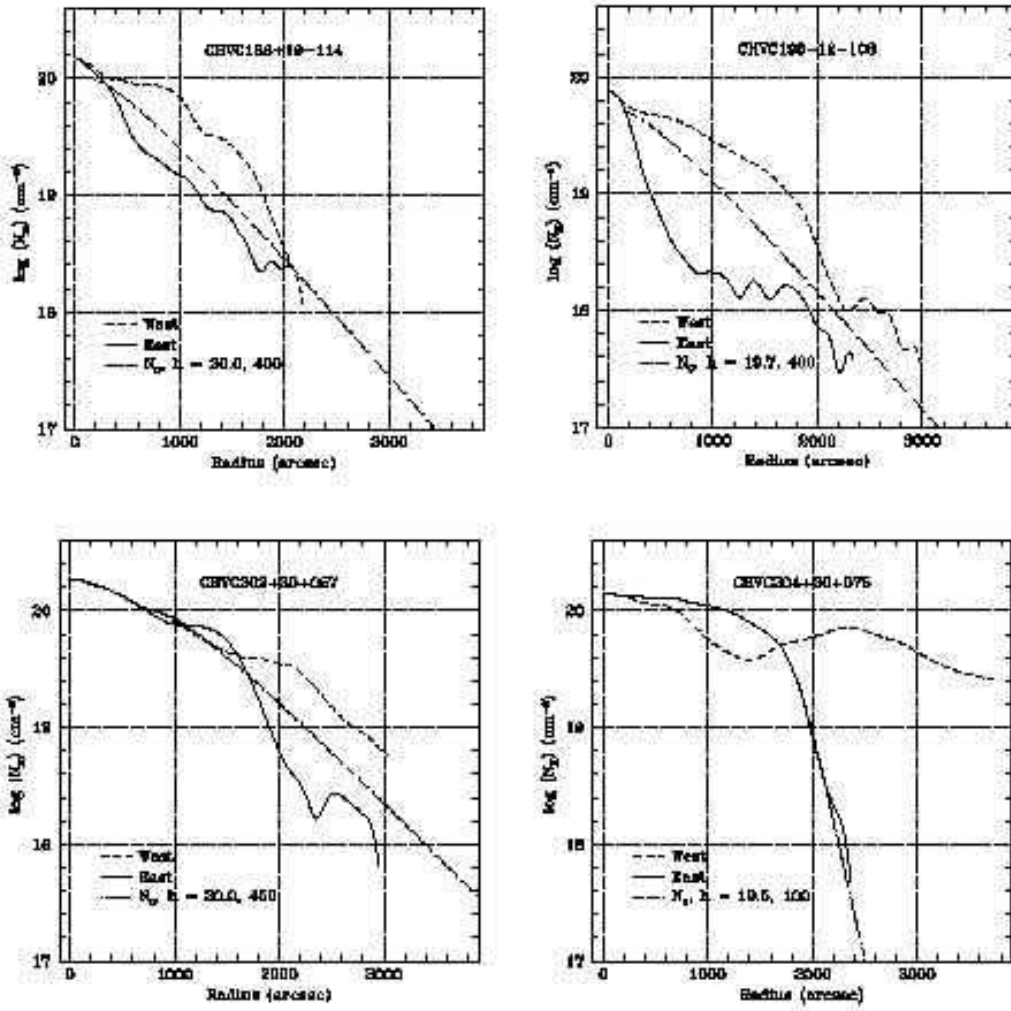
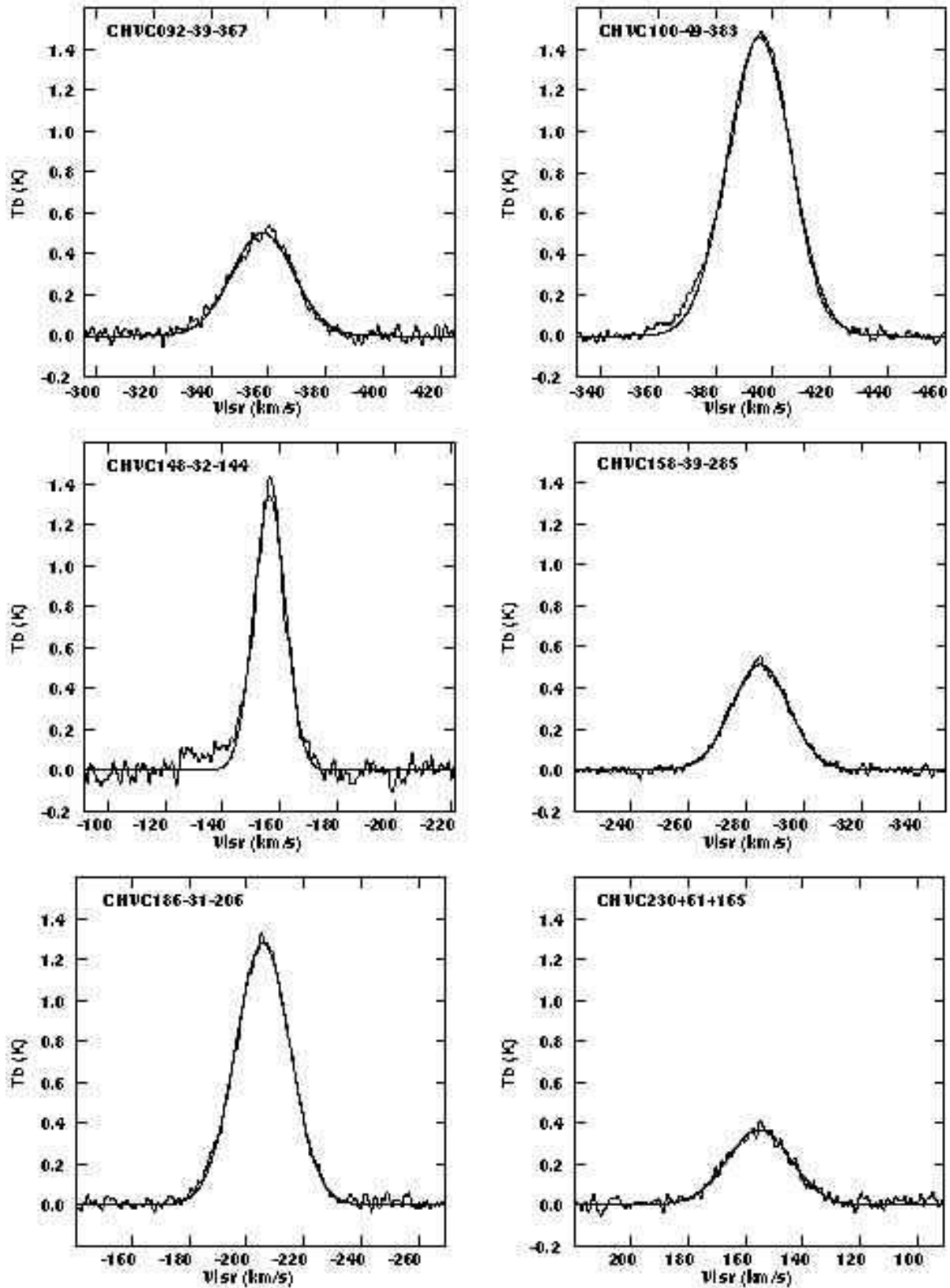


Fig. 12. Column density profiles of the indicated CHVCs as in Fig. 11.



**Fig. 13.** Spectra of the emission peaks in the indicated CHVCs. Each spectrum samples the emission peak in the lower-left panel of Figs. 1–10. Overlaid on each spectrum is the fit of a single Gaussian: the  $v_{LSR}$ ,  $T_{max}$ , and FWHM corresponding to this single Gaussian are tabulated in Table 2.

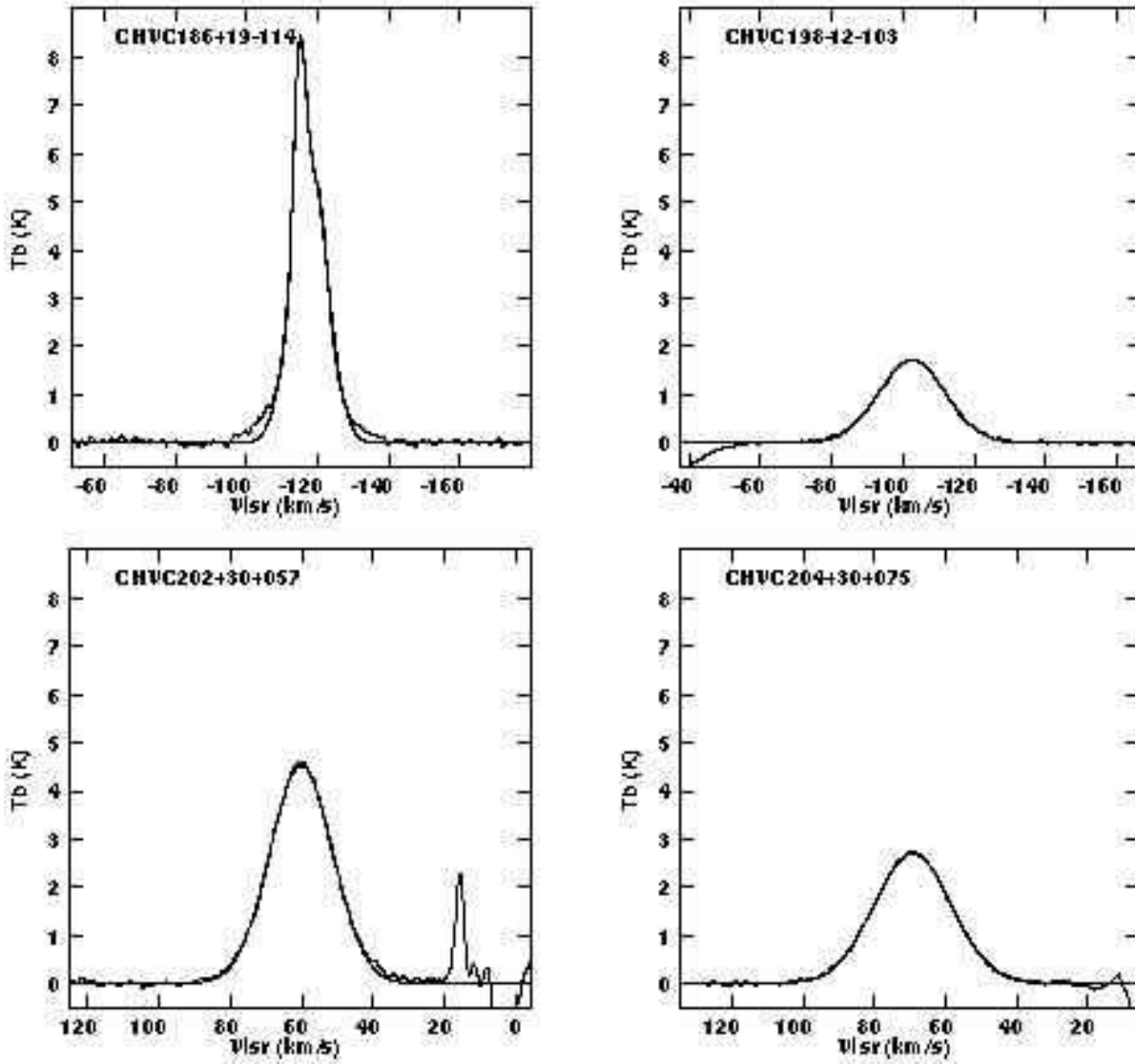
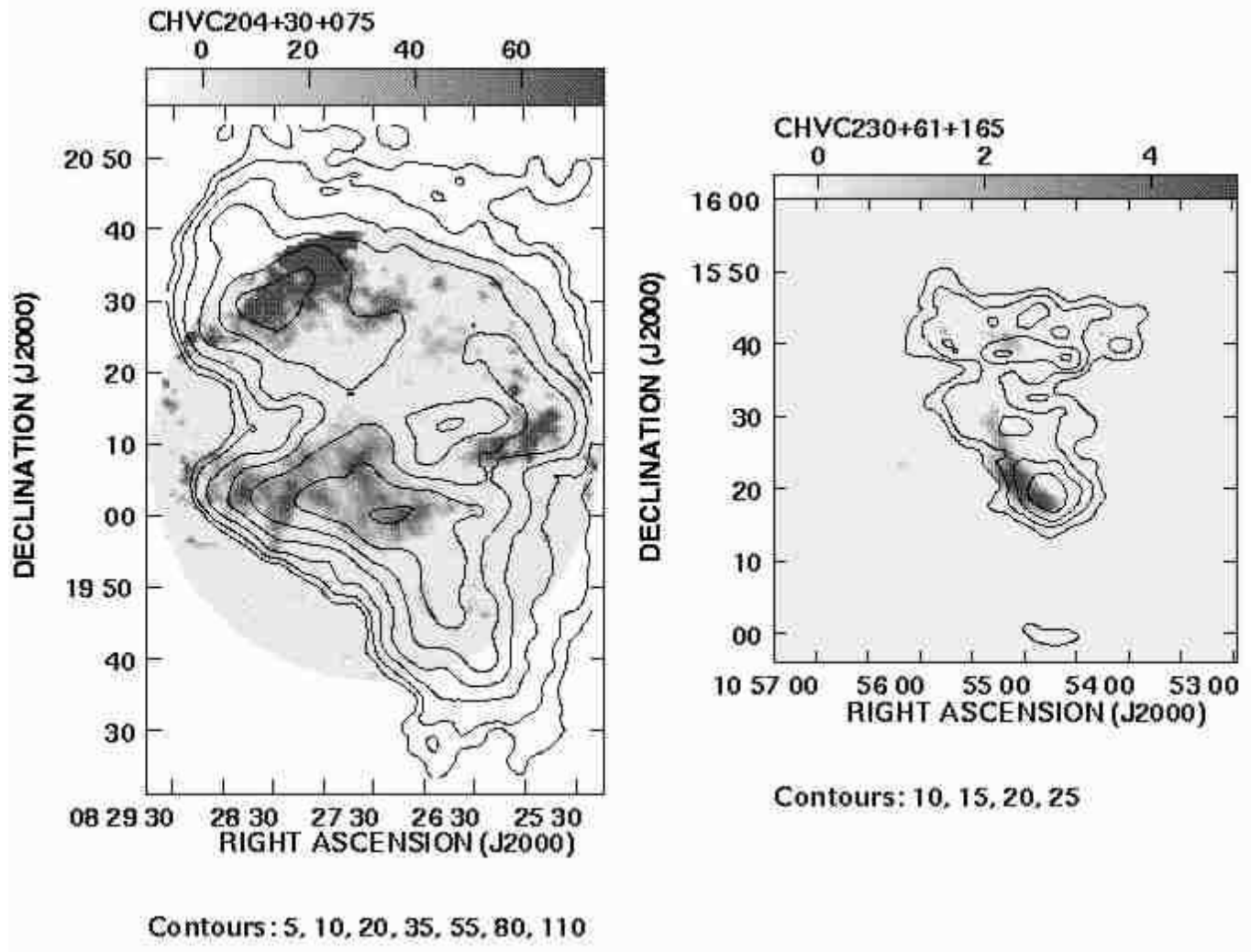
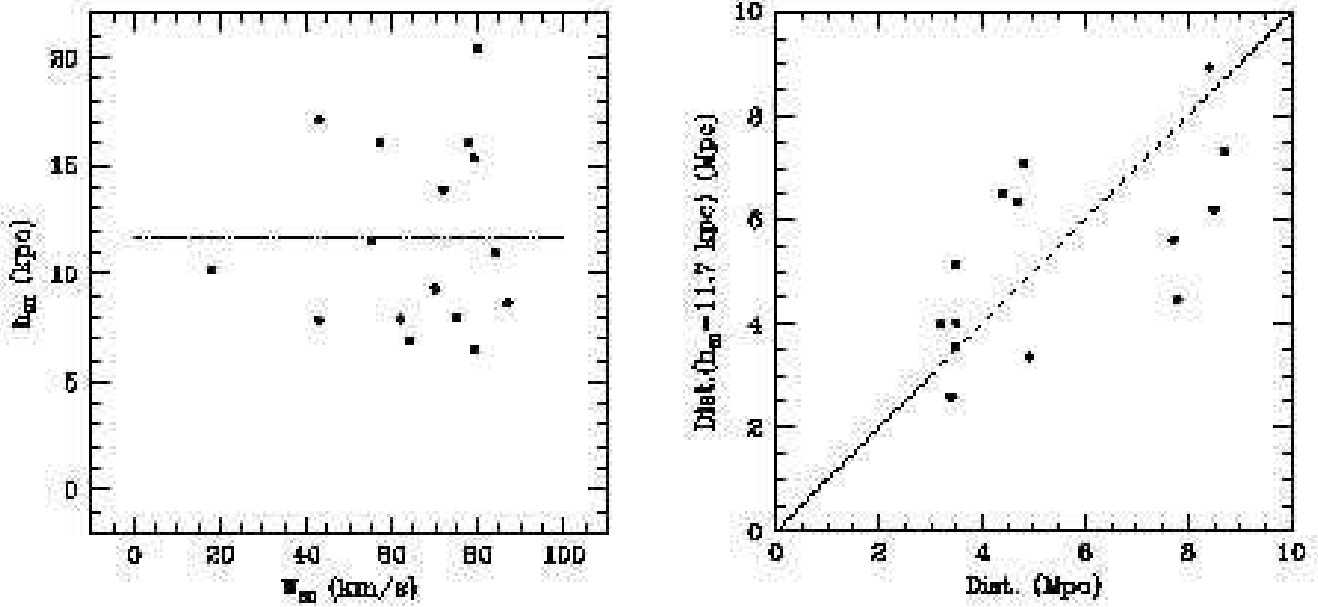


Fig. 14. Spectra of the emission peaks in the indicated CHVCs, as in Fig. 13. A single Gaussian resulted in an adequate fit for three of the objects, but not for CHVC 186+19–114, where the shape of the spectral cross-cut requires (at least) two components. The corresponding values of  $v_{\text{LSR}}$ ,  $T_{\text{max}}$ , and FWHM are tabulated in Table 2.



**Fig. 15.** Overlay of WSRT and Arecibo  $N_{\text{HI}}$  data for CHVC 204+30+075 and 230+61+165. The WSRT detected HI column density at 1 arcmin (for CHVC 204+30+075) and 2 arcmin (for CHVC 230+61+165) resolution is indicated by the grey-scale background. The Arecibo  $N_{\text{HI}}$  contours from Figs. 9 and 10 are overlaid.



**Fig. 16.** Outer-disk exponential scale-length of HI as a function of profile half-width in a sample of 15 nearby late-type dwarf galaxies taken from Swaters (1999) is indicated in the left-hand panel. The dotted line is the mean value,  $h_e = 11.7 \pm 4.4$  kpc. In the right-hand panel, the distance of the sample galaxies, derived assuming a constant intrinsic scale-length,  $h_e = 11.7$  kpc, is plotted against the optically measured distance. Equal distances would follow the dotted line. The actual distances are returned with less than a factor of two scatter by assuming  $h_e = 11.7$  kpc.